M-ARAMID NANOCOMPOSITE SEPARATORS FOR ENERGY STORAGE APPLICATIONS

A Dissertation
Presented to
The Academic Faculty

by

Michael Zhi-Hong Liu

In Partial Fulfillment
of the Requirements for the Degree
Master of Science in the
School of Materials Science & Engineering

Georgia Institute of Technology
May 2020

M-ARAMID NANOCOMPOSITE SEPARATORS FOR ENERGY STORAGE APPLICATIONS

Approved by:

Dr. Gleb Yushin, Advisor
School of Materials Science & Engineering
Georgia Institute of Technology

Dr. Preet Singh
School of Materials Science & Engineering
Georgia Institute of Technology

Dr. Yulin Deng
School of Chemical & Biomolecular Engineering
Georgia Institute of Technology

Date Approved: April 15th, 2020

823, always

ACKNOWLEDGEMENTS

I first and most importantly would like to thank Dr. Gleb Yushin for the oppurtunity to work in his lab during my time here at Georgia Tech. Dr. Yushin has shown me what it means to be a leader in the scientific space and demonstrated what it means to inspire others. He has also pushed me to become the best version of myself and to constantly question the boundaries to what I think I am capable of – I cannot be grateful enough for that. I hope to follow in his footsteps as I grow as a specialist in the battery field.

I also want to extend thanks to Jay and Kyle from Sila Nanotechnologies for our weekly discussion meetings. Their comments and suggestions about my project were helpful and constructive.

I also like to thank all of the staff at the Marcus Nanotechnology building: Eric Woods, Tim Zhang, Yolande Berta. Their expertise in characterization and willingness to troubleshoot right beside me helped me progress in my project faster than I could have alone.

Next, special thank you to the mentors that guided me during my time at Georgia Tech: Alex, Ani, and Dan. During times when I needed insight, they all reminded me of my North Star and my motivation to give all the effort I could no matter the task. I wish them nothing but the best in their bright careers.

Last, I want to thank my family, who are the foundation of who I am and became to be. Thank you for the constant support, and for being my #1 fans.

TABLE OF CONTENTS

LIST OF FIGURES

SUMMARY

Lithium-ion battery separators comprised of a nanocomposite of aramid polymer and alumina nanowires were presented as a new membrane architecture for more a thermally resistant and electrochemically superior alternative to the status quo. Porous membranes were produced by electrospinning low concentration m-aramid polymer (13%) with dispersed alumina nanowires. Resulting nanocomposite separators were non-woven mats that exhibited fast wettability, high integrity in thermo-gravimetric analysis tests up to 480 ºC, and less than 10% area shrinkage when exposed to temperatures up to 280 ºC. Physical, mechanical, thermal, and electrochemical figures of merit were discussed first from a practical standpoint then further examined in the context of the electrospun membranes. Results were contrasted with the performance of current state-of-art polyolefin separators. These m-aramid nanocomposite separators prove to be a strong candidate for batteries situated in demanding environments or large format batteries where safety is of paramount concern.

CHAPTER 1. INTRODUCTION

1.1 Forecast and Broader Context of Energy Storage

The landscape for global energy demand has drastically changed in the 21st century due to advances in energy generation and storage. According to a report from McKinsey on Global Energy Perspective, hydrocarbon-based energy production is expected to plateau by the year 2035[1]. The global use of coal has peaked in 2013, while oil and natural gas use is projected to peak at 2033 and 2037, respectively. The largest driver of this change arises from the infiltration of renewable energy sources in the form of wind, hydro, and solar power generation. These sources are set to comprise over 50% of the world's energy by 2035. Demand in vehicle electrification and building electricity retrofitting will lead development in renewable energy sources.

However, large scale development of renewable energy sources brings unique challenges. For instance, the solar industry has struggled to deal with the misalignment of the temporally limited nature of energy generation (e.g. only during daylight hours) and consumer electricity demand, which peaks in morning and again in the evening. The intermittent nature of consumer electricity load imbalance has infamously been given the term "duck curve" by its shape of demand versus time of day. Another resource from McKinsey, shown in Figure 1, depicts such challenge – during the hours of most intense daylight (between 11:00 and 16:00), the cost of producing electricity from photovoltaic solar power is low enough to displace all other forms of electricity generation[2]. Consequently, non-solar generation is reduced substantially for this period of time. During the evening, when electricity peaks, solar generation wanes and alternate sources of energy

generation must be fired up to meet demand. This volatility places a lot of strain on municipalities; some have resorted to using "peaker plants" which run on natural gas and/or dirtier coal to alleviate the load.

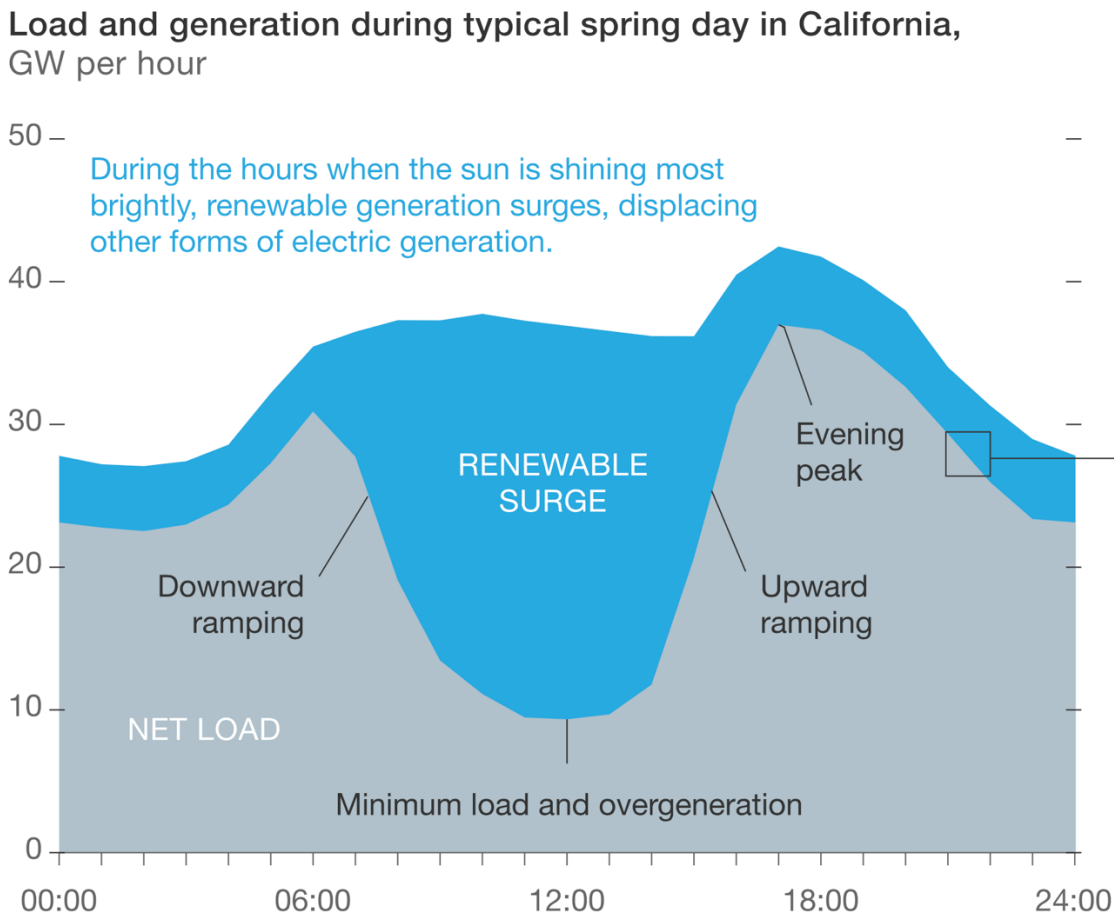

Figure 1: Illustration of the duck curve in electricity generation load caused by periodic consumer demand and renewable energy intermittency during daylight hours [2].

Industry has long searched for a solution to the intermittency and volatility of renewable energy. Of the possible solutions, lithium-ion batteries have been thrust into the spotlight due to their high energy density and relative efficiency. Storage of energy generated from solar and wind during peak generation hours can be stored in two mediums:

municipality-centered grid storage, or consumer electric vehicles. In the former, large plants of lithium-ion battery storage have been proposed to smooth out the load profile of non-solar generation by storing the energy locally and distributing it during peak times. In the latter, consumers owning an electric vehicle gain additional incentive from the municipalities to charge their vehicle during daylight hours in lieu of later in the evening during peak times. Electric vehicles have drawn considerable attention in comparison to grid storage, as they also serve to reduce greenhouse emissions plaguing current combustion engine vehicles.

Lithium-ion battery consumers have enjoyed an astronomical reduction in cost of ownership due to the increased demand (and thus increase in production capital investment) for such technology and the incessant incremental improvement upon energy density and efficiency. Cost of a battery pack as reported by Greentech Media (GTM) dropped from $550 to $236 per kWh from 2012-2017, which translates into a -16% CAGR, and is projected to decrease to $110 in the best-case scenario and $65 in the plausible best in class scenario by 2025[3]. This decline in cost will fuel the ubiquity of lithium-ion batteries both in grid storage and electric vehicles, even though higher energy density battery architectures are expected to debut in the future. Cautionary tales about battery safety, however, threaten this growth. Concerns about difficult-to-control battery fires caused by thermal runaway deter companies from adopting this technology. A report from Platts S&P Global cites that 23 recent battery fires have popped up from battery production facilities in South Korea due to this boom, while high-profile battery fires from electric vehicles make headlines due to safety concerns[4]. Producers of lithium-ion batteries must address

this issue to an adequate degree through fail-safe systems or innovations before the widespread adoption of large-scale battery systems.

1.2 Introduction to Lithium-ion Batteries

The development of the lithium-ion battery is rich in history, spanning over 40 years. One of the first reports of the potential for lithium as a secondary battery candidate material was the discovery that lithium ions could be electrochemically reacted to insert into the interplanar spaces of graphite. This discovery was made by Samar Basu at the University of Pennsylvania in 1977[5]. This discovery eventually led to the development of intercalation active materials at Bell Labs. In 1980, John Goodenough and Koichi Mizushima demonstrated that layered transition metal oxide materials also exhibited an electrochemical reaction with lithium at voltages near 4V vs. Li reference electrode[6]. With these two elements, the lithium-ion battery was made possible and was subsequently was commercialized by Sony in 1991. This discovery led to many more discoveries in the development of lithium-ion host materials for secondary batteries.

A lithium-ion battery consists of four major components: the cathode, anode, electrolyte, and separator (Figure 2). The first two components are the hosts of lithium-ions and are the components that dictate how much total energy capacity is possible per unit of measurement, while the latter two often dictate other important cell-level properties such as limiting current and coulombic efficiency. This section's aim is to introduce the first three components at a high level.

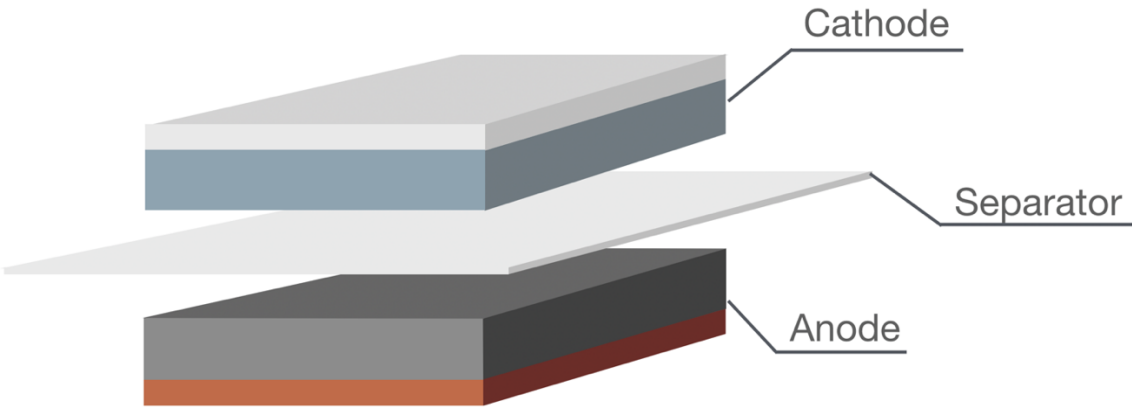

Figure 2: Illustration of a conventional lithium-ion battery stack. Electrolyte is filled between the cathode and anode to provide an ionically conductive medium.

The cathode of lithium-ion batteries consists of a thin foil of aluminum (typically 10-16 micron thick) with a coating of polymer and ceramic materials adhered to the surface and consisting of micron-sized ceramic "active" lithium ion storing particles, conductive carbon additives, and a polymer binder. State-of-art materials for cathode active materials include a mixture of transition metal oxide materials such as lithium manganese oxide, lithium cobalt oxide, or lithium iron phosphate[7]. The two general types of metal oxide active materials used in commercial batteries today are either of a layered or olivine structure. All these are considered intercalation materials: lithium ions occupy interstitial sites in these materials during discharge of the battery and leave said sites during charging. The specific capacity of Li storage in such material vary from around ~160 to ~200 mAh/g. However, there have been many advances in this field to expand the realm of materials that can reversibly hold and release lithium ions with higher densities. Though not discussed in detail here, new materials include classes of conversion-type materials (inducing a

breaking and reforming of bonds during electrochemical reaction) such as metal-halides and sulfur-based materials.

Anodes of lithium-ion batteries have a similar structure of cathodes: a metal foil (in this case, 8-16 micron copper) with micron-sized particles of active material, conductive additive, and polymer binder. State-of-art active materials for these electrodes include graphite and its variations, as carbon is one of the most abundant elements on Earth, is inexpensive, has reasonably high capacity (~360 mAh/g) and sufficiently low potential for reversible lithium intercalation to maximize lithium-ion battery cell voltage. There have been significant strides in the development of higher energy density anode materials. The most prominent alternative material is silicon, as it increases the anode specific capacity by roughly ten times[8-10]. Other areas of research interest include anodes made up entirely of lithium metal [11]; these electrodes are often paired with a solid-state electrolyte, as the lithium metal tends to form dendrites during the charging process.

The two remaining components of a lithium ion battery are the separator and the electrolyte. Commercial battery electrolytes consist of a mixture of organic solvents and a salt added and dissolved in such solvents for lithium ion conduction. Most electrolytes comprise of ethylene carbonate (EC) and diethyl carbonate (DEC) among other co-solvents with a $LiPF_6$ salt added[12]. EC with its high dielectric constant offers high salt solubility and forms a well-passivating layer on the graphite surface upon the initial electrolyte decomposition upon lithium-ion battery charge, but suffers from high melting point (+34 °C), while DEC co-solvent with a very low melting point (−74 °C) enables electrolyte operation at or below room temperature. Often, the inclusion of other solvent additives in

the electrolyte are important for desirable improvements in the long-term performance of the cell: these additives can have a great impact on the over efficiency of the cell[12].

1.3 Fundamentals of Electrochemistry in Context of Separators

Separators today are used as electrolyte reservoirs and enable ionic transport to drive the electrochemical reactions on each side of the cell. A separator's main function within an electrochemical storage system is to physically (electronically) separate the cathode and anode from each other to prevent self-discharge. Recently, two branches of research directions have gained significant interest in the lithium-ion separator field: solid-state electrolyte membranes (polymer and ionic) and high-performance porous separators which are filled with conventional liquid electrolytes. The former incorporates the separator within the electrolyte (as a solid phase electrolyte will physically separate the two electrodes and prevent them from shorting), while the latter seeks to improve the performance of such over conventional battery separators. Thermal shrinkage and mechanical strength stand out as critical factors for batteries in automotive applications and handheld devices, as shortcomings on either of those properties lead to immediate safety concerns.

The separator itself is a spectating component in the cell, e.g. it does not participate in any electrochemical reaction during charge or discharge of the cell. However, the structure, material, and properties of the separator can significantly affect the performance of the cell, as the separator can greatly influence the transport limitations and safety of the battery. Its effect on the transport of ions the electrochemical cell not only influences the

maximum limiting current in the system but also ultimately impacts metrics such as cycle life and apparent energy/power density.

The impact of separators in electrochemical performance stems from the increase in overpotential during operation, which causes the cell to reach its specified voltage cutoffs before full capacity utilization is reached. The observed voltage of an electrochemical cell can be described by the following relationship during discharge[13]:

$$V_{cell} = U^0_{cell} - |\eta_{ohmic}| - |\eta_{act}| - |\eta_{conc}|$$

in which

U^0_{cell} = the equilibrium cell potential,

η_{ohmic} = overpotential caused by ohmic contributions,

η_{act} = overpotential as a result of surface redox reaction kinetics,

η_{conc} = overpotential due to concentration effects

Each of these overpotential factors contribute to the reduction in the observed discharge capacity at a given current density. During charging (e.g. electrolytic reactions), similar penalties are applied as factors added to the observed voltage as opposed to subtracted. Electrode structure and active material selection most closely corresponds to activation overpotential contributions. Separators, on the other hand, impact ohmic and concentration overpotentials the most. To illustrate its impact, consider the potential gradient in electrolyte between two electrodes to sustain a specified current density, with the assumption that the potential behaves in an Ohmic fashion:

$$i_x = -\kappa \frac{d\phi}{dx}$$

in which

κ = ionic conductivity of the medium between the electrodes,

$\frac{d\phi}{dx}$ = potential gradient of electrolyte and separator

If we further assume that the potential gradient is linear within the electrolyte/separator medium, we come to the following:

$$\Delta\phi = \frac{iL}{\kappa}$$

in which

L = distance between the two electrodes,

$\Delta\phi$ = electrolyte/separator contribution to η_{ohmic}

The voltage penalty for ohmic contributions is thus inversely proportional to the ionic conductivity of the electrolyte-filled separator. Physical design parameters of the separator impact the corresponding ionic conductivity and will be later discussed in Chapter 2. From this relationship, it is also apparent that as current density increases, the voltage drop in the ionically conductive medium also increases proportionately.

Likewise, the separator also affects the concentration overpotential by impeding transport of cations within the electrolyte. Transport properties can be appropriately described by the combination of Nernst-Planck equation and Faraday's law as the sum of migration, diffusion, and conductive terms:

$$\mathrm{i} = -F^2 \nabla\phi \Sigma z_i^2 \mu_i c_i - F \Sigma z_i D_i \nabla c_i + F v \Sigma \mathrm{z_i} c_i$$

in which

i = current density,

F = Faraday's constant,

z_i = charge of the ion species i,

μ_i = mobility of the ion species i in electrolyte,

c_i = concentration of ion species i,

D_i = diffusion coefficient of ion species i,

v = molecular average velocity of fluid

The first migration term is derived from the forces of charged ions in the presence of a potential gradient. The second term, diffusion, is dictated by concentration gradients and the effective mobility of ions in movement. The last term, convection, relates the mechanical mixing of solution to its effect on transport. In a lithium-ion battery, we take convection as zero due to electroneutrality. The migration term can also be conceptualized as the following in absence of concentration gradients:

$$-F^2 \nabla\phi \Sigma z_i^2 \mu_i c_i = -\kappa \nabla\phi$$

In theory, the separator affects both the migration and diffusion term by reducing ionic conductivity and ion diffusion coefficients. It thus plays an integral role in determining not only the mass-transport controlled performance but also the limiting current of the system. Careful consideration of its impact on these two factors is essential when optimizing a membrane for electrochemical figures of merit.

1.4 Separator Design Strategies and Challenges

Separators also often serve as the crux of the measure of safety for an electrochemical cell – if the separator fails (e.g., due to a local temperature increase inducing reduction in the separator mechanical properties or separator shrinking, etc.), the electrodes may locally touch, inducing an internal short circuit, which in turn may cause a thermal runaway reaction. Two common methods on how to handle this failure mode exist: either 1) include a mechanism that prevents further electrochemical reaction to occur at higher temperatures (shutdown or closing the pores in the separator as the heat released from self-discharge when temperatures increase above some critical value), or 2) fabricate a battery separator that can withstand higher temperatures and can maintain mechanical stability, or 3) both (having a thermally stable base layer and a shutdown layer in the middle or on the top).

The most common mode for battery separators exposed to high heat is shrinkage – as the temperature of a cell increases, the polymeric film retracts to a less strained state due to entropy. This shrinking can be exacerbated as the temperature of the cell increases close to the glass transition temperature of the polymer used.

State-of-art separators are outfitted with a composite of polymer films to help mitigate this risk by of short-circuit by closing the pores that allow the electrochemical reaction to occur, effectively stopping the reaction. Separators such as Celgard's 3400 separator consists of a polypropylene-polyethylene-polypropylene trilayer composite. As the separator material experiences higher temperatures close to polyethylene's glass transition temperature, the middle layer closes out the pores allowing ions to flow through and blocks out ion transport[14]. As long as the polypropylene layers do not reach their glass transition temperature, the separator remains intact and prevents further catastrophic reactions to occur. This property has been named separator shutdown. However, it has been

shown that the effectiveness of the shutdown is highly dependent upon test conditions of the electrochemical cell – in some cases, it has been shown that currents upwards of 200mA (at 20 V) can still be passed through a shutdown separator[15]. A major limitation of current separators of this kind, however, is their limitation to current applications of consumer market batteries, which are smaller and have lower voltage (below 20 V). For large format electrochemical systems, this mechanism could also not be as effective in shutting down the cell.

The second method of preventing thermal runaway to fabricate a separator with high thermal stability. There are several approaches for increasing the thermal stability of separators. The first is to fabricate separators with more thermally stable polymers. Examples of such polymers with glass transition temperatures higher than polypropylene and polyethylene include polyimide and polyvinylidene difluoride (PVdF)[16,17]. The second is to create a composite material with ceramic additives to improve the thermal stability of the membrane. Additives such as aluminum oxide and titanium oxides are popular due to their abundance and price[18,19]. One major advantage of creating a composite material with ceramic additives is the ability to use a wide variety of polymers based on the electrochemical system needs – for example, if the cell required a particularly corrosive electrolyte, then creating a composite with a highly non-reactive polymer (such as polyvinylidene difluoride or similar) is possible. Additionally, the introduction of ceramic materials also increases desirable properties of the separator such as its wettability, ionic conductivity, and resistance to thermal shrinkage[20].

There are major advantages and disadvantages of the two described methods to mitigate the risk of thermal runaway in an electrochemical cell with the separator. An

argument for shutdown separators over high thermal stability separators is that lithium ion batteries generally lose a significant portion of their efficacy above 80ºC, and thus it would not be useful to allow further reaction above that temperature[7]. This argument holds true for cells of smaller size, but encounters more issues when dealing with larger scale systems, as these failed cells can still pass off non-negligible leakage currents[15]. The second method of fabricating more thermally stable separators strives to bridge the gap between current shutdown style separators and the demands of large format and/or novel battery chemistries.

CHAPTER 2. FIGURES OF MERIT AND LITERATURE REVIEW

As the fundamentals of separators has been established in chapter 1, this next chapter will continue on to further explore the concept of nanocomposite membranes and their potential. The first portion of this chapter will describe relevant metrics deemed important for separators, their impact on cell performance, as well as practical methods to measure such figures. The following section then will identify general separator architectures, the fundamentals of electrospinning, and the inspiration of this project to electrospin composite nanomaterials for membranes.

2.1 Separator Figures of Merit

A separator must meet a number of figures of merit to deem it as a possible candidate for use within an electrochemical system such as a LIB. These figures of merit can be broadly categorized in the following:

1. Physical/mechanical properties
2. Thermal properties
3. Electrochemical properties

Relevant figures of merit for physical/mechanical properties important to separator qualification include porosity, Gurley air permeability, electrolyte wettability, and tensile strength. Thermal figures of merit include thermal shrinkage below the separator's decomposition temperature and overall decomposition temperature among others. Finally, important electrochemical metrics to consider are ionic conductivity and effect on rate

capability. This section will examine these figures of merit to review what information each metric supplies.

2.1.1 Physical/Mechanical Properties

2.1.1.1 Porosity

The rudimentary measurement of battery separators physical characteristic can be measured in its porosity, a simple calculation of the ratio of empty space available within the separator volume compared to its total volume. It is the first and most important parameter of porous materials, given by the following unitless value[13]:

$$\epsilon = \frac{total\ volume - solid\ phase\ volume}{total\ volume}$$

Porosity can also be expressed with respect to the ratio between apparent versus true density of the material in question:

$$\epsilon = \left(1 - \frac{\rho_{app}}{\rho_{true}}\right)$$

in which

ρ_{app} = apparent density of the membrane,

ρ_{true} = true density of the membrane material

If the separator contains more than one material as a composite, then the following relationship holds:

$$\epsilon = \left(1 - \frac{\rho_{app}}{\sum x_i \rho_{i,true}}\right)$$

in which

x_i = the fraction of each component in the material,

$\rho_{i,true}$ = apparent density of the membrane

Common methods to measure porosity include direct density measurements by measuring the thickness and weight of a known area sample as well as measuring the weight of the separator before and after immersion into a liquid[21]. Design consideration of separator porosity is dependent on two factors: electrochemical performance and safety. Transport properties of ionically conductive media are reduced by the porosity of the solid phase within such media. In the case of a LIB, the effective ionic conductivity as well as the effective diffusion coefficient of an electrolyte-filled separator can be determined by the following relationship[13]:

$$\kappa_{eff} = \kappa_{bulk}\frac{\epsilon}{\tau} \quad , \quad D_{eff} = D_{bulk}\frac{\epsilon}{\tau}$$

where the bulk ionic conductivity and diffusion coefficient represent those of pure electrolyte and τ representing the tortuosity of the separator pores. This reduction in the effective conductivity can be translated back into the Nernst-Planck equation in absence of concentration gradients once more to obtain the following:

$$i = -\kappa_{eff}\nabla\phi$$

Alternatively, in the presence of concentration gradients, the following relationship holds:

$$i = -F^2 \nabla \phi \Sigma z_i^2 \mu_i c_i - F \sum z_i D_{i,eff} \nabla c_i$$

with the diffusion being affected by the separator due to its relationship with ionic mobility. From these relationships, it is clear that the microstructure and the openness of the separator's structure can greatly affect transport within the electrochemical cell and ultimately the ohmic and concentration overpotential losses associated with charge/discharge. From this perspective, it is most advantageous to design separators with as high of a porosity as possible; doing to will minimize the impact of the separator has on ohmic and concentration overpotential contributions. A low porosity membrane limits the transport of lithium ions during electrochemical processes, forcing the system to reach specified voltage cutoffs though impedance losses. However, high porosity membranes also pose an apparent safety risk: their mechanical strength is reduced compared to that of an impermeable membrane due to the decrease in cross-sectional area caused by pores. Mechanical failure of membranes has a high likelihood of causing short-circuiting within a cell and subsequent risking of thermal runaway. In addition, it is commonly observed that high porosity membranes have worse shrinkage characteristics at high heat. A proper medium of these two factors must be struck based on the intended application of the separator.

2.1.1.2 Gurley Air Permeability

Practically, there exists a number of methods to determine the porosity and tortuosity of a separator. Most often, the MacMullin number is used to determine the ionic conductivity of the separator. The MacMullin number correlates the resistance of the separator immersed in liquid electrolyte to the resistance of the electrolyte without the

separator. This ratio is fairly easy to determine, as the MacMullin number is proportional to the air permeability of the membrane. The most common method to measure the air permittivity of a membrane is through measuring the Gurley value[22], which is a measure of how much time it takes for 100 cubic centimeters of air to pass through a unit area with a constant pressure applied[23]. This method is experimentally the easiest to find with a lower chance of error. The Gurley number of a separator also correlates with its ionic conductivity in solution, making it a viable metric to gauge a separator structure's effect on cycling performance.

2.1.1.3 Wettability

Another important figure of merit for battery separators is electrolyte wettability. As the electrolyte is the sole conductor of current between the two electrodes in a battery, rapid adsorption and retention of electrolyte from the separator is required to minimize its impedance impacts on the system[24]. From a processing standpoint, a high electrolyte wetting rate accelerates the filling speed of the electrolyte within a battery, reducing dead time during production. Separator wettability depends not only on physical characteristics such as thickness, porosity, and pore size, but also other factors such as the surface energy and hydrophobicity[25]. Often, this metric is measured as the relationship between the area of a membrane wetted with a known volume of electrolyte with respect to time.

2.1.1.4 Tensile Strength

From a mechanical perspective, a battery separator needs to have a high tensile strength either isotopically or in the direction of which it is wound into rolls for processing. This direction (e.g. the direction of movement in a roll-to-roll process) is denoted as the

machine direction, while the direction perpendicular denoted as the transverse direction (TD). As previously stated, when design a separator, there exists a tradeoff between electrochemical performance and tensile strength based on the porosity of the membrane. When the porosity increases in a separator, the fraction of air in its cross-sectional area increases accordingly, leading to more stress applied to the solid phase for an observed cross-sectional area. Thorough consideration of this tradeoff is essential for choosing an appropriate membrane porosity. Additionally, the metric of puncture strength according to a standard (such as ASTM D3763). Dimensionally, it is generally accepted that a thinner separator is beneficial for electrochemical performance (less ohmic drop across the electrolyte phase) but detrimental to safety due to the risk of defects/punctures occurring for thin separators. State-of-art battery separators usually have pores smaller than 1 um to allow electrolyte to flow while blocking larger particles from migrating from electrode to electrode. Typical battery separators in commercial production aim to be around 20-25 microns in thickness to optimize this tradeoff[26]. Measurement of the ultimate tensile strength, strain, and Young's modulus follows the general relationship during a uniaxial tensile test:

$$\sigma_{UTS} = \frac{F}{A}$$

$$\epsilon = \frac{\Delta L}{L_0}$$

$$E = \frac{\sigma(\epsilon)}{\epsilon} = \frac{F/A}{\Delta \mathrm{L}/\mathrm{L}_0} = \frac{FL_0}{A\Delta L}$$

in which

F = force exerted at break point,

A = cross-sectional area of membrane,

ΔL = change in specimen gauge length from the origin,

L_0 = gauge length original length

2.1.2 Thermal Properties

2.1.2.1 Shrinkage

One of the most critical safety criteria to meet for membranes in electrochemical systems is area shrinkage at elevated temperatures. This metric is simply taken as the area at any given time of a thermal heat soak test compared to the original area of the separator. Shrinkage undermines a separator's fundamental purpose to create physical space between the two electrodes in the system by exposing both electrodes to potential contact. In practice, the risk of shrinkage or misalignment in the battery winding process leads to excess separator along the electrode edges to outline potential electrode sections from touching, lowering the volumetric and gravimetric energy density of the overall system. Additionally, separator shrinkage and deformation at low to moderate temperatures below 100ºC generally limit the ability to expel moisture from the separator. Trace amounts of water in fluorine-based electrolyte salts have been shown to produce hydrofluoric acid during cycling which leads to current collector corrosion and active material degradation[27]. Thus, for safety and long-term electrochemical performance, design of separators should prioritize minimizing thermal shrinkage. A commonly cited minimum requirement for thermal shrinkage states less than 5% over 60 minutes at 90ºC; however, higher

temperatures are welcome and will likely positively impact long term performance while providing a larger safety net for high-temperature operation[24].

2.1.2.2 Thermal stability

At even higher temperatures, the decomposition temperature of the separator enters the discussion as another thermal figure of merit to measure. In present day, a LIB risks thermal runaway if the cell overheats and short circuits. Opportunities for this to occur start near the glass transition temperature of the membrane (for polyolefin-based membranes, about 120ºC) but have a guaranteed failure rate at the membrane's decomposition temperature. This decomposition temperature is most often determined through thermogravimetric analysis (TGA) in air, where the point during the temperature sweep where a majority of the weight fraction of polymer decomposes into carbon dioxide and other gases.

2.1.3 Electrochemical Properties

2.1.3.1 Ionic conductivity

Separators must physically separate the electrodes while allowing ions to flow between the cathode and the anode to properly function as an electronically insulating medium between the positive and negative electrodes of a LIB. The electrochemical system is unable to produce work in electrons flowing through the external load if the separator failed to do so, as the redox reactions would self-discharge (e.g. short circuit) otherwise. The electrochemical metric to measure the admittance of ions, ionic conductivity, is a function of a number of factors such as species of electrolyte, concentration of ions,

temperature, and porosity of membrane among others. As admittance is inversely proportional to resistivity, this metric can be experimentally determined by measuring the bulk resistance of a symmetric blocking electrode cell and normalizing this value by the electrode interface area and distance between the two electrodes. It is assumed in this method that the ionic conductivity of the electrolyte is much lower than the electronic conductivity of the blocking electrodes and thus is the limiting factor in the measurement. The bulk resistance of the symmetric cell can be found from the x-intercept of a potenitostatic EIS sweep from high to low frequency. The ionic conductivity of the electrolyte can then be found with the following relationship:

$$\kappa = \frac{d}{R_{bulk}A}$$

in which

κ = ionic conductivity,

d = distance between the two electrodes (thickness of separator),

A = area of blocking electrode

It is also clear from this relationship that the thickness of the separator is paramount in reducing the ohmic contributions of the cell. From a design standpoint, the separator must be as thin as possible to minimize the bulk resistance applied to the system. There is additional motivation to decrease the separator thickness from a packaging/energy density perspective: in a fixed volume system, energy density should theoretically increase if the inactive material volume fractions (separator, metal foils, conductive binders, and more) are minimized. However, as previously mentioned, reducing the thickness of the separator

increases the risk of mechanical failure during processing, requiring more delicate processes to manufacture cells. Additionally, thinning out a separator reduces its ability to block lithium dendrites from penetrating from the anode to the cathode to cause short-circuits[28]. As with porosity, determining appropriate separator thickness involves considering trades between cell performance and mechanical integrity/processability.

2.1.3.2 Rate capability

Perhaps the biggest impact that a separator has on electrochemical performance of a cell is its impact on rate capability. Though rate capability is a common figure of merit for membranes, it is rather a culmination of a number of factors previously mentioned such as porosity and ionic conductivity. A simple ratio of the charge/discharge capacity of a high current density cycle over that of a low current density cycle (specified as the control current density) gives a relative comparison of rate capability:

$$rate\ capability = \frac{C_{high\ i}}{C_{low\ i}}$$

The difference in capacities observed in each of these cycles, as previously mentioned, arises from the increased voltage penalty of inducing a larger current density of the electrochemical system, causing the system to reach specified cut-off potentials sooner than when cycled at a lower current density.

2.2 Separator Architectures

Generally, one can divide the trending classes of separator research into 1) microporous separators[29-32], 2) modified microporous membranes[25,33,34], 3) composite

membranes[35-37], 4) electrolyte membranes[38-41], and 5) non-woven mats[42-45]. Microporous separators are classified by their pore size in comparison to some of the other separators mentioned. Modified microporous membranes encompasses the previous classification with significant surface modifications such as plasma, irradiation, or additional polymer coatings. The third classification of composite membranes encompasses variations of 1) and 5) by introducing inorganic ceramic materials to bolster the properties of the polymer base. Electrolyte membranes encompass all materials that simultaneously serve as the separator and the ionic conductor for the electrochemical cell. Finally, non-woven mats represent membranes produced by entangling fibers into a web-like structure to form a separator with rather high porosities. This work will focus on developing membranes based on a non-woven mat architecture.

2.3 Electrospinning Fundamentals

Electrospinning is a fiber spinning method that has gained considerable attention in the recent decade due to its ability to produce ultrafine fibers and their mats from either a dispersed polymer solution or a polymer melt[46,47]. These ultrafine fibers can be collected during deposition to produce a non-woven mat with remarkable properties. In principle, electrospinning draws out fibers from a spinneret tip by overtaking the forces of surface tension by inducing a large voltage gradient between the spinneret tip and a grounded current collector. When a critical voltage is reached, thin fibers are pulled to the grounded current collector in an anisotropic manner based on environmental conditions in which the fibers are drawn in. While solution-based electrospinning has been the most popular method of creating these ultrafine fibers, gel-electrospinning and/or electrospinning from

a polymer melt have recently been developed to garner ultrafine fibers with outstanding tensile and toughness properties[48-50].

Electrospinning comprises of an electrodynamic process in which an electric field is applied to a droplet of polymer solution to elongate and stretch it into a continuous stream of ultrafine fiber[51]. A typical electrospinning setup consists of a high voltage source, a syringe pump, syringe of polymer solution, a spinneret, and a collector as depicted in Figure 3. During the process, the polymer solution is extruded from the tip of the spinneret at a controlled rate. The spinneret tip is connected to the positive lead of the high voltage source, where a positive bias is applied. Conversely, the collector is connected to the negative terminal and acts as ground. When a critical voltage is applied, the droplet of polymer distorts, indicating that the electrostatic forces exerted upon the droplet have overcome the surface tension of the polymer solution[52]. As this polymer jet is drawn to the collector, it undergoes rapid contortions due to the instability of the stream, elongating the stream into sub-micron proportions. As the stream approaches the collector, the polymer starts solidifying due to the solvent evaporation and increased surface area of the polymer-air interface and leads to the deposition of a mat of fibers on the collector. To further examine this process, one can examine the distortion of the droplet due to an imbalance in exerted force. The shape exhibited by the distortion of the solution is often termed as the Taylor Cone[53-55]. Formation of this cone can be described as a force balance of applied voltage and the surface tension

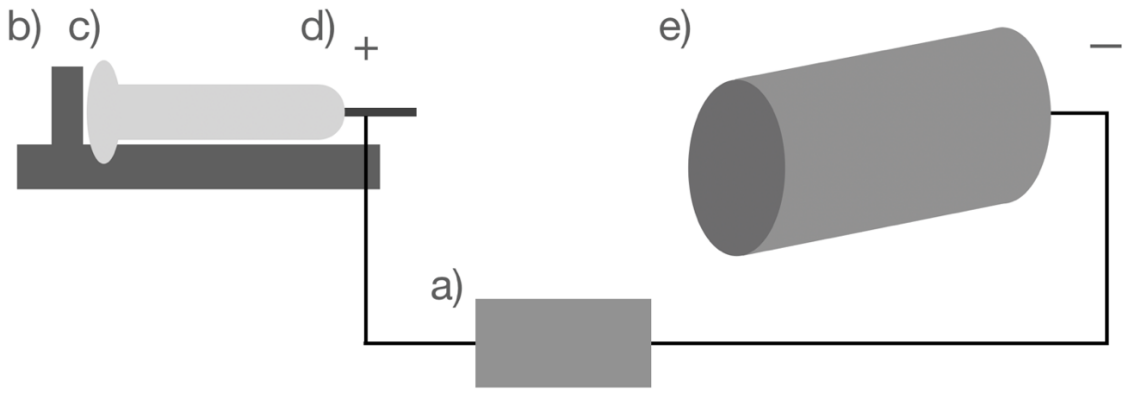

Figure 3: Schematic of a typical electrospinning setup consisting of a) high voltage source, b) syringe pump, c) syringe of polymer solution, d) spinneret, and e) collector.

as described by the following equation relating the critical voltage with deposition parameters[56]:

$$V_c = \frac{4H^2}{h^2}\left(\ln\left(\frac{2h}{R}\right) - 1.5\right)(1.3\pi R\gamma)(0.09)$$

in which

H = distance between tip of spinneret and collector,

h = length of spinneret,

R = outer radius of spinneret,

γ = surface tension of polymer solution

This relationship demonstrates that the critical voltage required to induce the Taylor Cone is dependent upon the geometry of the deposition setup as well as the interface properties of the polymer solution. Continuing on from the Taylor Cone, the stream of polymer continues for a certain length in a straight line as it is accelerated by the electric field. This

section before it starts bending and whipping is typically approximated by the following relationship:

$$L = \frac{4\kappa Q^2}{\pi \rho^2 I^2}\left(\frac{1}{R_0^2} - \frac{1}{r_0^2}\right)$$

in which

$R_0^2 = \left(\frac{2\sigma Q}{\pi \kappa \rho E}\right)^{\frac{1}{3}}$

σ = surface charge of the polymer

Q = flow rate of solution

κ = electrical conductivity of the solution

ρ = density of the solution

E = electric field strength

I = current passing through jet

r_0 = initial radius of jet

After this region, the stream gradually loses acceleration from the electric field until it reaches a constant velocity. Any small perturbation at this point will induce instability in its trajectory, which will in turn begin to whip the fiber back and forth. This motion dramatically thins the fiber diameter in the "instability region." The amount of fiber draw is dependent upon a number of factors including surface tension of the stream, viscosity of the solution, dielectric constant, flow rate, and electrical current of the process. The terminal diameter of the polymer jet is projected by the following:

$$d_t = \left(\gamma\epsilon\left(\frac{Q}{I}\right)^2 \frac{2}{\pi(2ln\chi - 3)}\right)^{\frac{1}{3}}$$

in which

ϵ = dielectric constant of the fluid surrounding the jet,

χ = dimensionless parameter describing the wavelength of the bending instability

The resulting thinned out stream is thus what is deposited on the collector. A flat, non-woven network of polymer fibers is produced from this process that returns the high surface area of the individual fiber strands. Given the proper parameters, these relationships give a solid foundation in which to initial electrospinning parameters off of for a given polymer solution. Deposition parameters could then be adjusted appropriately based on empirical findings.

2.4 Electrospinning in Context of Battery Separators

Electrospinning has found a niche in battery separators, as this method is able to produce mats of polymer separators with a large open structure[24]. The wide selection of polymers available for electrospinning allow different separators to be produced for different battery applications. Previous efforts in this field have garnered battery separators that revolve around the safety of the lithium-ion battery system that it is placed in. For example, Wang et al. demonstrated that composite separators can be produced through electrospinning polyimide with nano-silica particles embedded in the fibers[17]. The resulting membrane exhibited a large increase in porosity (90%) as well as a substantial increase in electrolyte uptake (reported as 2400%). Wang et al. chose polyimide due to its

high thermal stability – this composite material was thermally stable up to 250ºC[17]. Another example of electrospinning as a cutting edge method of producing high-performance separators was the spinning of core-shell microfibers with a thermal-triggered flame retardant by Liu et al[57]. This "smart" separator had triphenyl phosphate imbedded inside the separators as a thermal runaway inhibitor – if the cell temperature reached a critical melting point for the PVdF host, then the flame retardant would be released and would stop the flammable organic solvents from catching fire. Though these two examples use electrospinning as the main production method for separator synthesis, the method to inhibit thermal runaway are much different.

One limitation worth noting about electrospinning is its limited ability to be scaled up for mass producing membranes. Typically, this technique uses a needle to disperse ultrafine fibers onto a current collector: this process is slow compared to the many industrial processes available to produce microporous membranes. Recent efforts have, notwithstanding, begun to improve electrospinning deposition rates to what is required for industrial applications. For example, Forward et al. demonstrated that an electrostatic jetting from a free liquid surface was possible, exponentially increasing the rate at which ultrafine fibers can be produced[58]. However, this technology still falls shy from commercialization and needs further advancement before electrospinning could be considered viable on any large scale. In addition, needles could be assembled into regular arrays of 1,000-1,000,000 needles for up to 1,000-1,000,000 increase in the spinning rate. In order to increase the solvent evaporation rate in such needle arrays, the hot air may be injected around the fibers in a concentric manner, similar to the industrial spray-pyrolysis setups.

2.5 Proposed Work of Electrospinning Aramid Polymer Separators

Promising research directions of electrospun materials for battery separators could move towards higher performance polymers as the backbone of the separator. Of the aforementioned metrics for battery separators, aramid polymers are of great interest due to their high thermal stabilities, robust mechanical properties, resistance to chemical degradation, and high hydrophilicity among other advantageous characteristics[59]. The aramid polymer family are polymers derived from nylon; however, these polymers contain aromatics in their backbone (hence the nomenclature of aramid). The addition of aromatic monomers in the backbone substantially increases the strength of these chains as a higher proportion of the chemical bonds contribute to the stiffness of the polymer backbone[60]. The two most prominent aramid derivatives are *p*-aramid and *m*-aramid (Figure 4). They are differentiated by the positions of the substituent bonds on the aromatic compounds, e.g. bonding of the backbone occurs in the *para* and *meta* configuration, respectively. The two major companies who have developed these materials are DuPont in the United States and Teijin in the Netherlands. Both types of fibers maintain mechanical strength, even at higher temperatures. The thermal stability of aramid macrofibres has been reported up to 476ºC and 521ºC for m-aramid and p-aramid, respectively, and mechanical strength up to 860 MPa and 3600 MPa from Teijin[61].

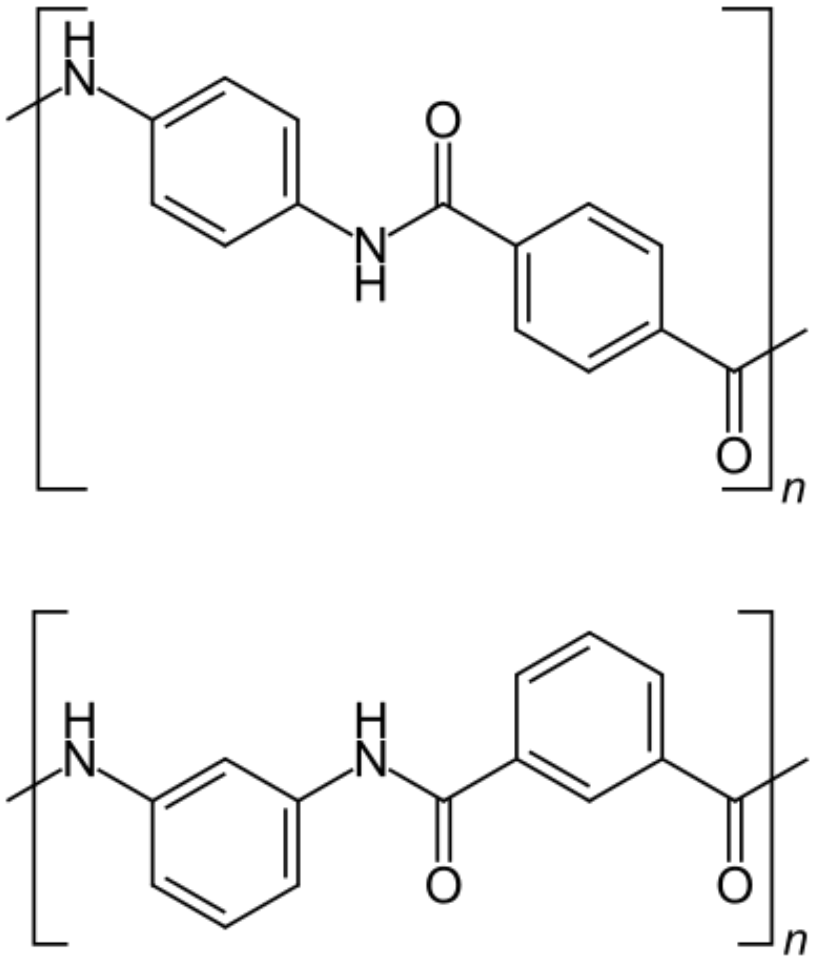

Figure 4: Chemical structure of aramid polymer chain repeat units in the a) para and b) meta bonding configurations.

Although *p*-aramid generally exhibits superior mechanical and thermal properties over m-aramid, its extreme chemical resistance results in incredibly difficult process conditions to make it viable for electrospinning. Currently, the only known method to solution process this polymer is through immersing the polymer in concentrated sulfuric acid (100%); this is the standard solution that both DuPont and Teijin use to produce their branded Kevlar and Twaron materials respectively. Such processing is often discouraged

for a large-scale production material due to worker safety concerns and cost of equipment to minimize chances of hazardous and dangerous accidents. There have been efforts to produce a Kevlar electrospun membrane; however, electrospinning was not used to produce the membrane and could only produce a stringent amount of fibers during the process [62].

On the other hand, *m*-aramid is relatively easier to process, as it is dispersible in organic solvents such as N, N-Dimethylacetamide (DMAc) and Dimethylformamide (DMF) with the addition of lithium chloride (LiCl). This processability comes at a cost of a moderate reduction of mechanical and thermal properties. Previous efforts to electrospin m-aramid have determined that the addition of lithium chloride is essential to dispersing the aramid polymer chains, as the chlorine ions attract to the chains through intermolecular bonding and disrupt the intermolecular forces that hold the solid fiber together [63]. A schematic of this interaction between chlorine ion and m-aramid is presented in Figure 5. Without this ion-polymer interaction, polymer solvation within DMA would not be possible due to the strong IMF forces of m-aramid polymer chains, which also give the polymer its superb resistance to chemical attack and high stability in electrochemical environments. Earlier efforts to electrospin *m*-aramid have been successful, and applied to structural composites to increase mechanical properties[64]. Lee et al. demonstrated that battery separators indeed could be produced with a high decomposition temperature and respectable mechanical properties[65]. However, characterization of thermal, mechanical, and electrochemical performance seems incomplete for pure m-aramid membranes. There remains much more opportunity to explore the possibility of using m-aramid in electrospun

membranes with a full suite of characterization. Based on this finding, *m*-aramid could potentially serve as a high-

performance backbone for a composite separator combining a ceramic additive to further enhance m-aramid's electrochemical and thermal strengths.

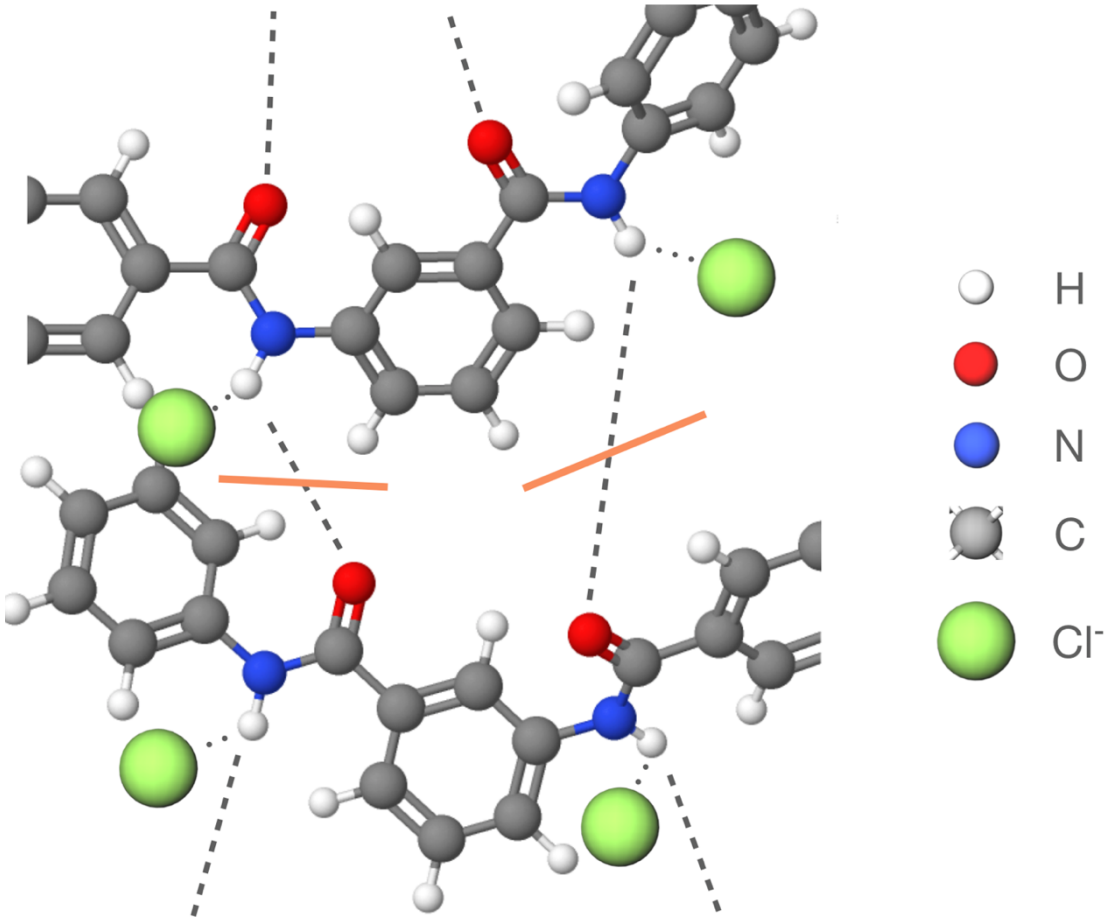

Figure 5: Conceptual depiction of the role chorine ion has on disrupting Van der Waals interactions (in orange) between m-aramid chains. Orientations and spacings are not exact and are for illustrative purposes only.

CHAPTER 3. NANOCOMPOSITE M-ARAMID/ALNW SEPARATORS FOR LITHIUM-ION BATTERIES

3.1 Introduction

Lithium-ion batteries have sustained international research attention due to their promise of high energy density amid falling costs for large format grid storage of electricity[66]. As the power of computing and vehicle electrification races forward, the energy consumption in order to power those commodities will increase accordingly. It is then unsurprising that a significant portion of research effort has been continually devoted to increasing the energy density of these storage systems. However, as one increases the energy density of a cell, one also increases the capacity for severe and dangerous failures to occur. The safety of lithium-ion batteries and other high energy density storage systems must be investigated accordingly.

Of the four different components in an electrochemical cell (cathode, anode, electrolyte, separator), the separator is most directly linked to safety. Different strategies are used to minimize the risk of a battery short circuiting itself to cause a catastrophic thermal runaway reaction. One method is to increase the polymer separator's thermal stability to withstand abuses of high temperature. Many strategies exist to fabricate novel and high-performing separators including multi-layer composites[35-37], separator composites with inorganic additives[25,33,34], and higher heat tolerance polymer constituents[42-45]. Of these strategies, incorporating nanomaterials and nanostructures seem to hold one of the most promising routes to increase separator performance.

1D materials such as nanorods, nanowires, nanotubes, and more have attracted great attention for their ability to magnify the conductive, strength, and transmission properties of wide-reaching classes of materials[67,68]. Traditionally, synthesis routes for 1D nanomaterials require significant cost or effort to produce them in useful quantities. However, recent advances in synthesis techniques provide methods to produce these materials much less prohibitively, opening up new opportunities to use these materials in applications previously unconsidered. For example, Lei et al. demonstrated a direct transformation of bulk alloys into oxidizable aluminum alkoxide nanowires by dealloying in simple organic solvents through strain minimization[69]. This breakthrough in materials synthesis allows alumina nanowires to be incorporated in architectures like battery separators without significant cost to enhance membrane properties such as wetting and thermal stability.

Aramid polymers are also well known for their superb thermal stability, mechanical strength, resistance to chemical attack, and resistance to abrasion[70]. Derivatives are widely used in demanding use cases such as flame-resistant suits for emergency rescue personnel and ballistic vests[71]. Poly(m-phenylene isophthalamide) (hence PMIA or m-aramid) is an aromatic polyamide that exhibits decomposition temperatures as high as 476ºC and in some cases a higher strength-to-weight ratio than steel[72,73]. M-aramid is also solvated in an ionic liquid of LiCl mixed within DMA; in contrast, other aramid polymers (such as p-aramid) are only solvated in highly hazardous 100% sulfuric acid. In addition, m-aramid has shown promise in nanomaterials synthesis, as it is compatible with electrospinning.

The combination of this high-performance polymer with alumina nanowires provides an opportunity to create a nanocomposite material with superior performance and

rational cost. Herein we present a separator design rationale based on the synthesis of a nanocomposite membrane through electrospinning of m-aramid and alumina nanowires which exhibit dramatically increased thermal and electrochemical performance compared to common polyolefin separators used commercially today.

3.2 Experimental Section

3.2.1 Materials

Poly(meta-phenylene isophthalamide) (m-aramid, TeijinConex) staple fiber was purchased from Teijin. N, N-Dimethylacetamide (DMAc, ReagentPlus®, ≥99%) was purchased from Sigma-Aldrich. Lithium chloride (LiCl, anhydrous, 99%) was purchased from Alfa Aesar. Alumina nanowires (AlNW) were obtained from American Elements. All materials were dried in a vacuum oven at 120ºC for 2h before making solution.

3.2.2 Preparation of m-aramid solution for electrospinning

To prepare solutions to electrospin, LiCl was quickly added to DMAc (2 wt. % of the total solution weight) by stirring at ambient temperature for 2h to prevent unwanted moisture absorption. Once the solution was clear, AlNW (1 wt. % or 2 wt. % relative to the total solution) were added and sonicated using a Misonix ultrasonic tip for 2 minutes modulated at 15W to evenly disperse the AlNWs. Then, m-aramid staple fibers were added (13 wt. %) and vigorously stirred at 80ºC for 16h until the neat m-aramid solution was clear and/or there were no visible fibers left within. Viscosity measurements were taken with a viscometer (Brookfield Engineering) at 3.0 RPM with the temperature of a 2.1mL sample controlled at 25 ± 0.2ºC with a water bath.

3.2.3 Fabrication of electrospun m-aramid membranes

Electrospinning solutions (0, 1, 2 wt. % AlNW) were placed in a 10 mL syringe outfitted with a 10G flat-tipped needle. The electrospinning setup used consisted of a syringe pump (New Era Pump Systems, Inc.), commercial DC high voltage source (Gamma High Voltage Research), and a rotating drum collector. Electrospun mats were produced on aluminum foil collectors with a 25 kV bias, a tip-to-collector distance of 15 cm, feed rate of 0.1 mL/hr, and 300 RPM rotating speed for the drum collector. The environment of the electrospinning setup was controlled to 45 ± 5% relative humidity and 20 ± 2ºC. After deposition, the resulting mat was submerged in a bath of deionized water at ambient temperature for 4h before drying at 165ºC for another 4h to evaporate water and DMAc.

3.2.4 Physical characterization of m-aramid membranes

Separator porosity was calculated by measuring the thickness and weight of a 2.85 cm^2 disc of the electrospun mat to obtain its apparent density and dividing by the true density of the membrane. The Gurley number (air permittivity) was measured using a Gurley 4110N densometer with a 2.54 cm diameter orifice. To obtain more consistent measurements, the average of 300cc of air passing through the membrane was taken over 3 trials for each membrane thickness. Scanning electron microscopy (SEM, Hitachi SU8010) was used to determine average fiber diameter distributions of membranes tested (N = 32). Transmission electron microscopy (TEM, FEI Tencai F30) was used to reveal the internal structure of an individual fiber of the electrospun mats and the relative AlNW distribution within the fiber. The ultimate tensile strengths of the membranes were

measured by testing a dogbone specimen cutout compliant to ASTM 8110 standards on a tensile testing machine (Mark-10) outfitted with a 25N load cell and a crosshead speed of 2mm min^{-1}. The gauge length of the specimen used was 15mm and the width was 3mm. Electrolyte wettability investigations used commercial ethylene carbonate:diethyl carbonate electrolyte (1M $LiPF_6$ in EC:DEC 1:1 by volume) as the wetting liquid in 2 μL volumes. Images were taken of the 1.98 cm^2 membrane disk every ten seconds after placement of the electrolyte onto the center of the film. The total area wetted was measured using ImageJ.

3.2.5 Thermal characterization of m-aramid membranes

Thermal gravimetric analysis (TGA, Mettler Toledo) was used to determine the decomposition temperature as well as the experimental weight fraction of AlNW within the membranes. Samples were first heated in air to 165 ºC and held for 20 minutes to expel any excess moisture or solvent from electrospinning. Then, after returning to ambient temperature, measurements were taken at a ramp rate of 10 ºC min^{-1} in the same atmosphere. Thermal stability tests were conducted at temperatures varying from 25-300ºC in air. Samples were loaded into a kiln (SentryXpress 4.0) for 2 minutes at the specified temperature. Thermal shrinkage tests were conducted in a similar manner with the exception that each sample was held at temperatures ranging from 25-300ºC in 20ºC increments for 1 hour. Images were taken both before and after heating and the resulting area of each membrane was evaluated using ImageJ.

3.2.6 Electrochemical characterization of m-aramid membranes

Electrochemical studies were performed in CR2032 coin cells with 1M $LiPF_6$ in EC:DEC 1:1 electrolyte. Ionic conductivity measurements were found using a symmetric coin cell with stainless steel electrodes, taken from electrochemical impedance spectroscopy (EIS) on a Gamry Reference 600+ (Gamry Instruments, Inc.). Potentiostatic impedance studies were conducted within frequency range of 1 MHz to 100 Hz at a 10 mV amplitude. Temperatures were controlled using a Tenney environmental control chamber in the range of 25-60ºC during these studies to a ± 0.3ºC accuracy with a 1hr heat soak time before each measurement. Polarization studies were conducted with a full cell consisting of a commercial graphite anode (MTI Corp) paired with a commercial NCM-523 cathode (MTI Corp). Both electrodes were vacuum dried 120ºC before transferring into the glove box for coin cell assembly. The areas of both electrodes were kept equal in this full cell study as other works have recommended. Charge-discharge tests were performed using an Arbin battery cycler.

3.3 Results and Discussion

Figure 6 shows a summary of the effect of adding AlNWs into the electrospinning solution on solution viscosity, fiber diameter, and calculated porosity. Neat, 1% AlNW, and 2% AlNW membranes (from weight fractions of electrospinning solution) herein are designated as A0, A1, and A2. The addition of 1% and 2% AlNW weight fraction in solution correspond to theoretical weight percentages of 7.69% (~7.5 wt. %) and 15.38% (~15 wt. %) in the solid electrospun membranes, respectively. Measurements taken from a viscometer show that the addition of AlNWs monotonically increased solution viscosity from 6132 cP to 10447 cP. The increase in viscosity of the solution could be attributed to

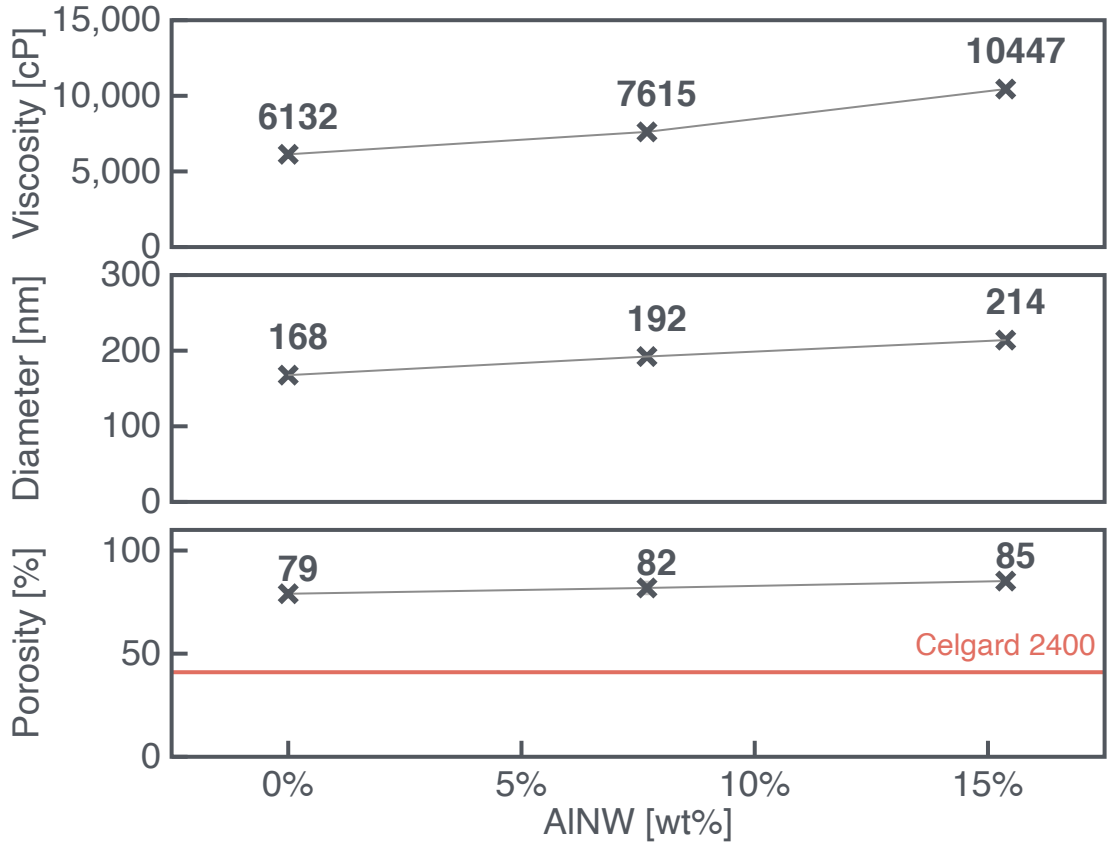

Figure 6: Summary of selected properties of m-aramid solutions and membranes spun from those solutions. Weight percentage of AlNW in the horizontal axis corresponds to the theoretical percentage found in the membrane with respect to m-aramid:AlNW ratio, and not that of AlNW in solution.

the increase in solids to solvent ratio with the addition of AlNWs. As established in previous electrospinning studies, this increase in viscosity of the solution increases fiber diameter of the electrospun membranes due to the decrease in fiber elongation during the fiber draw process in the instability whipping zone. In Figure 7, scanning electron microscopy (SEM) reveals that the mean of the fiber diameter distribution also increases as more AlNW is added to the electrospinning solution. Electrospinning neat, 1% AlNW,

and 2% AlNW m-aramid solutions garner 168, 192, and 214 nm average fiber diameters, respectively. Additionally, images of transmission electron microscopy (TEM) highlight the morphological difference between neat electrospun m-aramid membranes and membranes with added AlNW. Figure 8 shows individual electrospun fibers from a 0% AlNW membrane and a 15% AlNW membrane in panels (a) and (b). AlNW nanowires average about 300nm in length and are oriented co-axially within the m-aramid fiber in a similar morphology to what is observed in composite material extrusion printing[74].

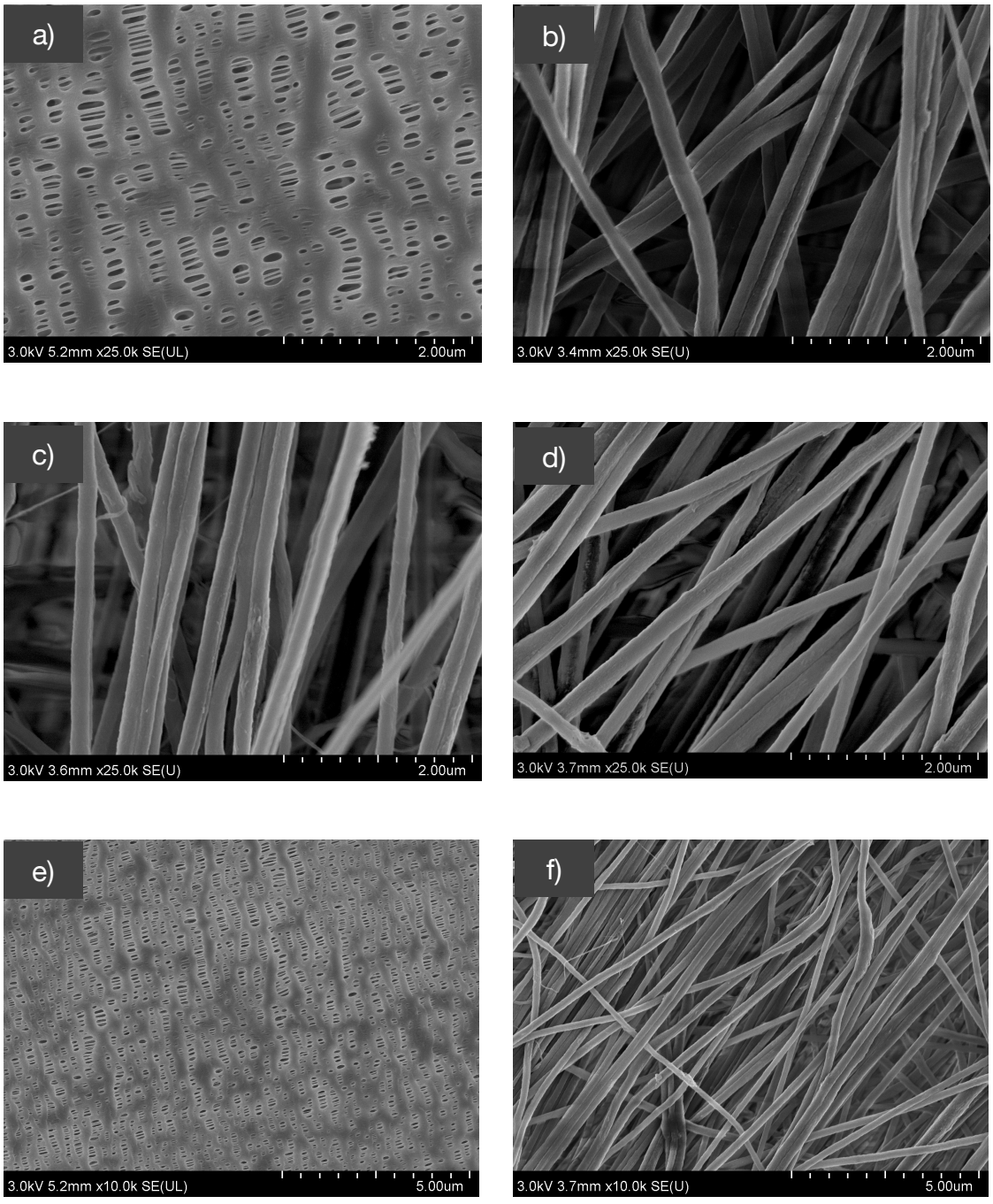

Figure 7: SEM imaging of separator membrane samples: a) Celgard 2400, b) 0 wt.% AlNW, c) 7.5 wt.% AlNW, d) 15 wt.% AlNW, e) Celgard 2400 at x10K, and f) 15 wt% AlNW at x10K.

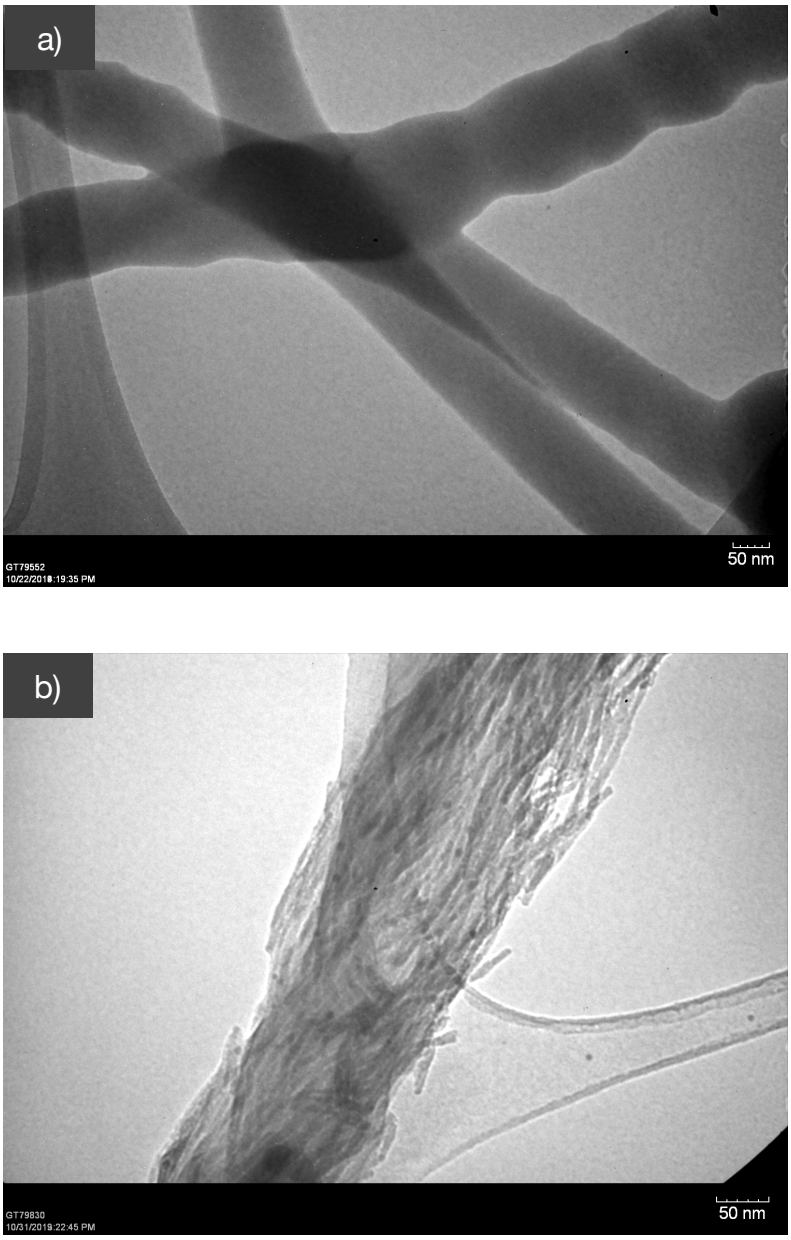

Figure 8: TEM imaging of single strands of fiber electrospun from 0 wt% AlNW and b) 15% wt. AlNW samples.

It is worth noting that as m-aramid and the LiCl required to solvate such within DMA are highly hydrophilic, the relative humidity of the electrospinning environment has significant impact on the alignment of fibers during the electrospinning process. As relative

humidity increases, electrospun fibers align more to the circumferential axis of the rotating drum collector. This phenomenon can be explained by m-aramid's high hydrophilicity/low solubility in water and the solvent DMA's high miscibility with water. A higher relative humidity during the electrospinning processes promotes early phase separation of polymer with its solvent compared to other polymer-solution systems. A relative humidity of 45 ± 5% was experimentally determined for this study to balance the degree of fiber alignment with membrane reproducibility.

Also as expected, this increase in average fiber diameter affects the average porosity of each membrane. Large diameter fibers are more difficult to pack efficiently in space; this results in an increase in void spaces within the membrane that allow for higher porosity. Calculated porosity from thickness and weight measurements shown in Figure 6 reiterate this point in showing that the porosity of electrospun membranes increase by a marginal amount from 79 to 85% porous from 0 to 15 wt.% AlNW concentrations respectively. A commercial single-layer uniaxially elongated polypropylene separator (Celgard 2400), in contrast, show a porosity of 42%. The impact on electrochemical performance from this difference in porosity between the control and electrospun membranes is further discussed in the following sections. The increase in porosity also is correlated with a decrease in mechanical strength. As shown in Figure 9, the mechanical strength declines from 61 MPa to 31 MPa when comparing A0 to A2. However, the 15% AlNW membrane sample exhibited a higher ultimate tensile strength compared to other cited electrospun work for energy storage applications[57,65,75].

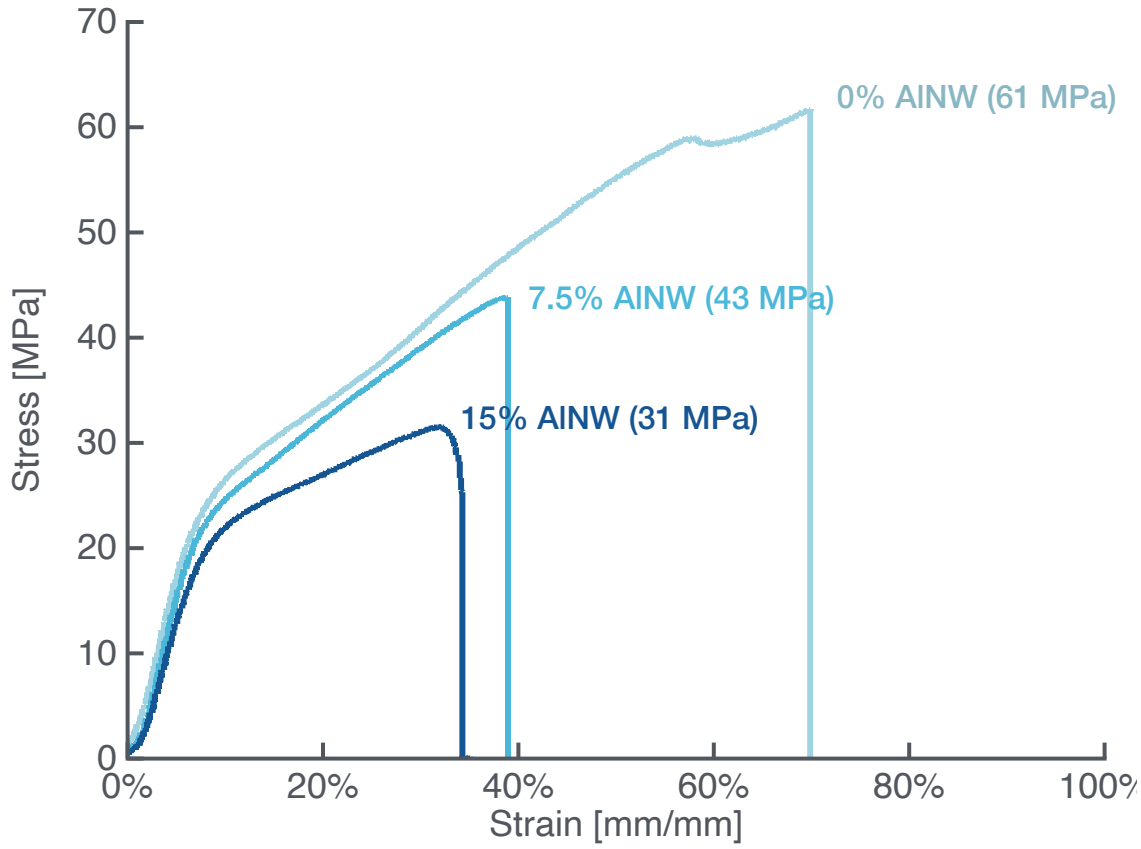

Figure 9: Stress-strain curves of 0% AlNW, 7.5% AlNW, and 15% AlNW membranes.

A separator's primary purpose in the electrochemical system is to ensure that the cathode and anode do not make contact with one another in various operating conditions while minimizing its impact on impedance of the overall system. Cycling at elevated temperatures poses the most risk with thermal stability and shrinkage as figures of merit. First, thermogravimetric analysis (TGA) in air was used to compare the decomposition temperatures of the m-aramid membranes compared to that of the polypropylene control. In this study, the decomposition temperature of a membrane is defined as the point at which the membrane loses 10% of its total mass. TGA curves as shown in Figure 10 depict a thermal decomposition temperature for the polypropylene control at approximately 280ºC

while all m-aramid membranes decompose at 450ºC. The addition of AlNWs do not alter the decomposition temperature of the electrospun membranes but rather vary the amount of remaining material after combustion. The weight percentages of AlNW to m-aramid found in the 7.5 and 15% samples through this method (6.3% and 12.7%) were within reason to theoretical values. A membrane's practical thermal stability limit is determined by its glass transition temperature, where significant shrinkage or pore-closing occurs. Thermal stability tests as shown in Figure 11 show that at the PP control experiences extreme shrinkage at as low as 150ºC for a brief exposure of 2 minutes; by 200ºC, the PP membrane crosses its glass transition temperature and shrinks into a solid mass of polymer. In contrast, the electrospun m-aramid fiber membranes maintain their integrity until 300ºC past their 272ºC glass transition temperature. The membranes were also exposed to a heat soak of temperatures ranging from 25-300ºC for 1h to quantify the amount of shrinkage experienced at elevated temperatures as depicted in Figure 12. The control PP membrane shrank below 90% of its original volume by 120ºC and steadily decreased in total area by 160ºC, after which the separator would no longer effectively partition any portion of the cathode and anode in an electrochemical system. In contrast, the m-aramid membranes maintained close to 100% of their original area for temperatures up to 220ºC. In this range, the addition of AlNWs had little influence on membrane integrity, as m-aramid demonstrates excellent stability. After this threshold, the relative areas of each membrane decrease with the final area correlating to the percentage of AlNWs added. The membrane spun with 15% AlNW maintains more than 90% of its original area at 260ºC just before the glass transition temperature, in contrast to the 72% of original area maintained by the neat m-aramid membrane. Adding AlNW into a neat m-aramid electrospinning solution

greatly improved shrinkage performance of the membrane. However, this improvement was met with a diminishing return with an excess of AlNWs added (14% improvement versus 18% improvement when comparing A1 and A2 to A0, respectively). The resistance of shrinkage at temperatures close to the glass transition temperature of m-aramid can be explained by two factors. First, the decomposition temperature of Al_2O_3 greatly exceeds that of m-aramid at over 2000ºC. In tandem, the integration of AlNWs within the individual strands of m-aramid fibers retard the morphology change of these fibers when exposed to temperatures near m-aramid's glass transition temperature. This resistance to deformation under heat is thought to be especially robust in this architecture, as the AlNWs are impregnated within the fiber itself as opposed to being applied to pure m-aramid membranes as a coating.

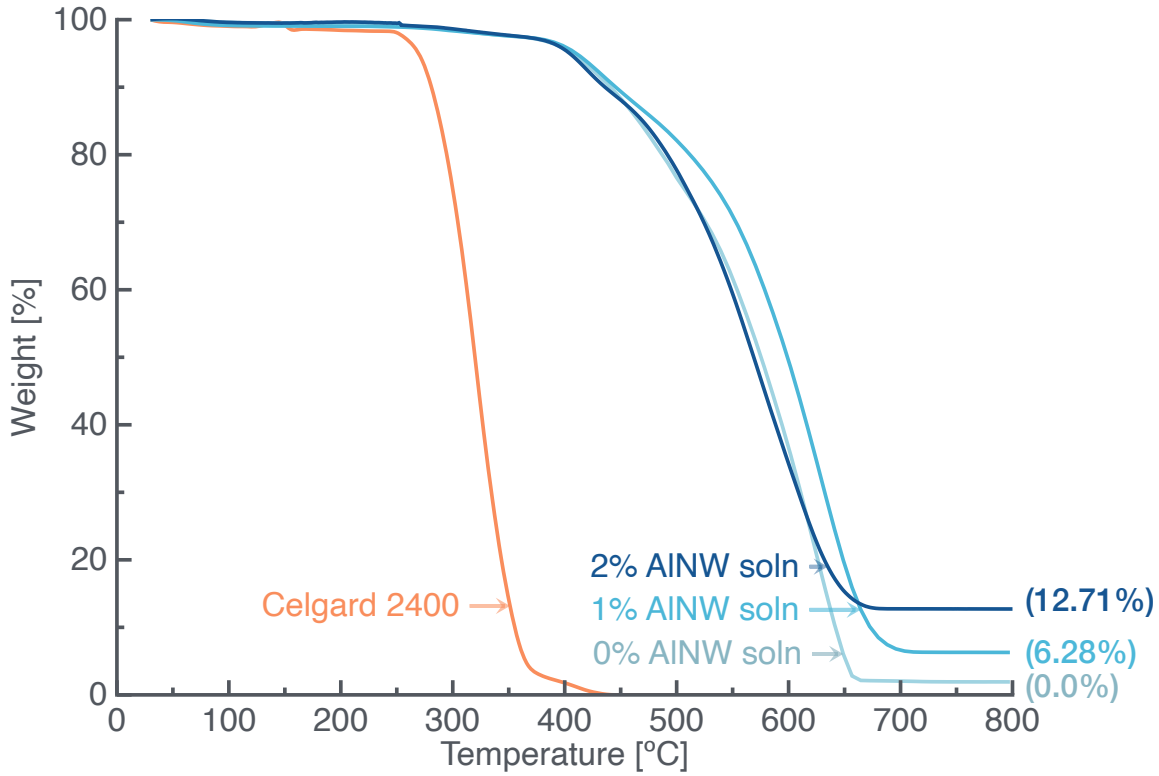

Figure 10: TGA curves of Celgard control, 0% AlNW, 7.5% AlNW, and 15% AlNW in nitrogen atmosphere. Samples were heated at a 10°C/min rate.

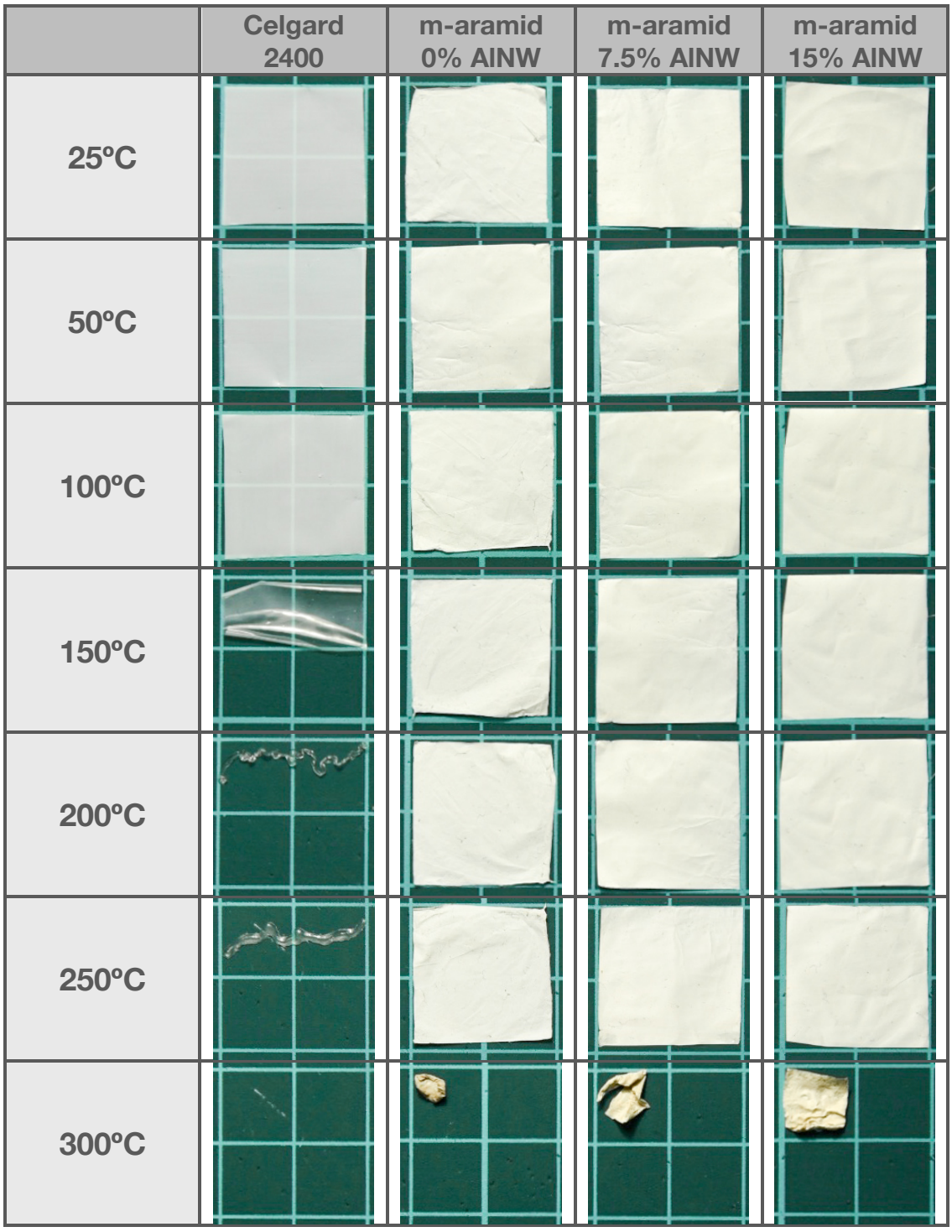

Figure 11: Flash heat soak test for thermal stability of Celgard control, 0% AlNW, 7.5% AlNW, and 15% AlNW in air. Samples were heated for 2 minutes.

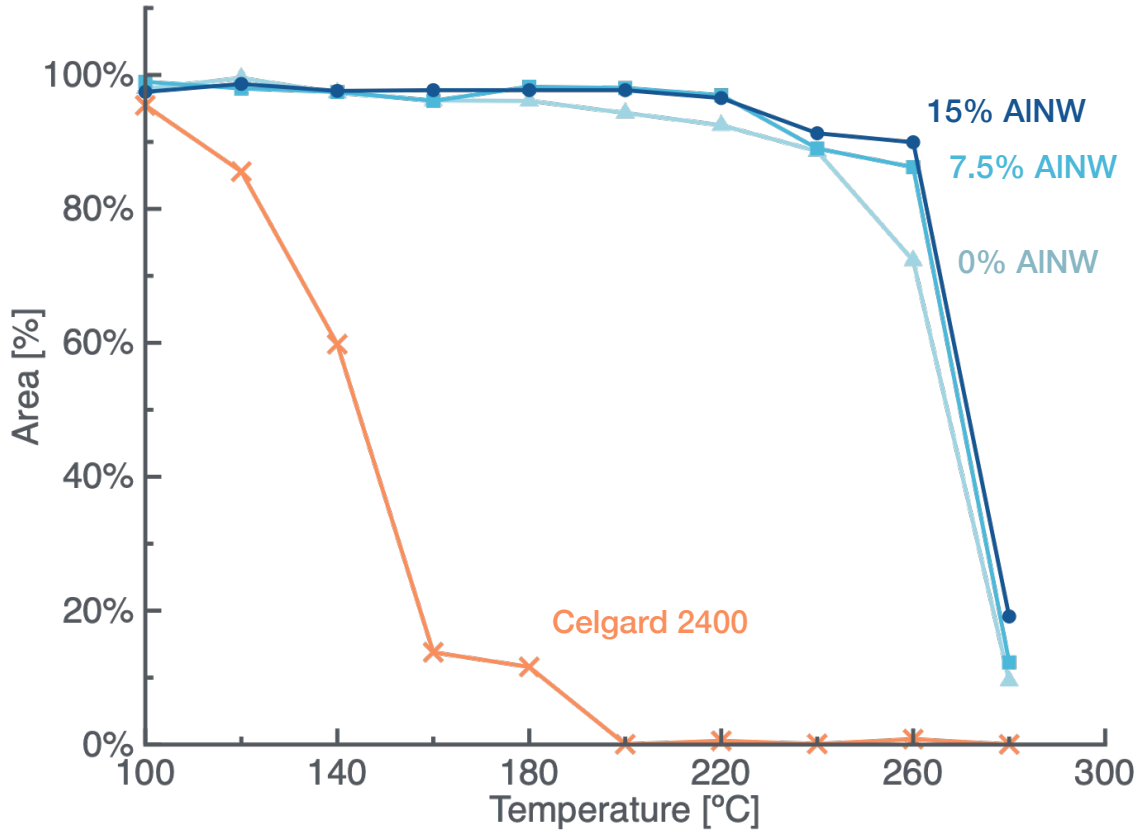

Figure 12: Heat soak test for thermal shrinkage of Celgard control, 0% AlNW, 7.5% AlNW, and 15% AlNW membranes. Samples were annealed for 1 hour in air with an original 2 cm² area.

Nanocomposite m-aramid/AlNW membranes not only exhibited superior thermal resilience over their polypropylene counterpart but also demonstrated a marked improvement in electrochemical performance. Membranes mostly contribute to impedance (and subsequently electrochemical performance) through affecting the ionic conductivity within the electrolyte phase. Gurley air permittivity tests were first conducted to evaluate the inferred difference in performance between the control and electrospun membranes. Normalized values were found with respect to membrane thickness for appropriate

comparison as in Figure 13 and Figure 14 under the assumption that the relationship between membrane thickness and discharge of fluid per unit of time were directly proportional (e.g. Darcy's law remained valid). The normalized Gurley air permittivity of A0, A1, and A2 membranes of 0.28, 0.26, and 0.16 s/μm respectively were determined to inversely correlate with AlNW weight percentage. This finding is in accordance with the higher calculated porosity measurements for membranes with increasing weight percentages of AlNW. We hypothesize that this relationship corresponds to the larger average diameters of m-aramid/AlNW composite fibers, resulting in higher volume fractions of void space within the membranes. It is also possible, that the composite fibers were stiffer (less compliant and deformable) and thus packed less densely on the collector surface. In comparison, the average normalized Gurley air permeability of the polypropylene control was considerably higher at 20 s/μm, following its lower calculated porosity. These air permeability results were expected to correlate with ionic conductivity within an electrochemical system, with a higher normalized Gurley number resulting in decreased conductance capability. Direct ionic conductivity measurements were taken by performing EIS with symmetric stainless-steel electrode coin cells to evaluate the electrochemical performance of these membranes in carbonate-based electrolyte. Figure 15 depicts the typical relationships between ionic conductivity and temperature for each of the membranes. Though all separators exhibited an increase of ionic conductivity as test temperature increased, the m-aramid membranes consistently showed superior ionic conductivity compared to that of the polypropylene control throughout the temperature range of 25ºC to 60ºC. At room temperature, the 15% AlNW membrane showed close to 3 times the ionic conductivity of the control (2.72 mS/cm compared to 0.950 mS/cm).

Additionally, the introduction of AlNWs in the membrane also increased the ionic conductivity in the entire spectrum of temperatures tested. Improvements in ionic conductivity were most apparent when comparing the family of electrospun m-aramid fiber membranes to the control polypropylene membrane: the pure m-aramid membrane sample demonstrated over 90% improvement. Within family, the addition of AlNWs enhanced this improvement by up to another approximate 60% (from 1.82 mS/cm to 2.72 mS/cm comparing A0 and A2 samples).

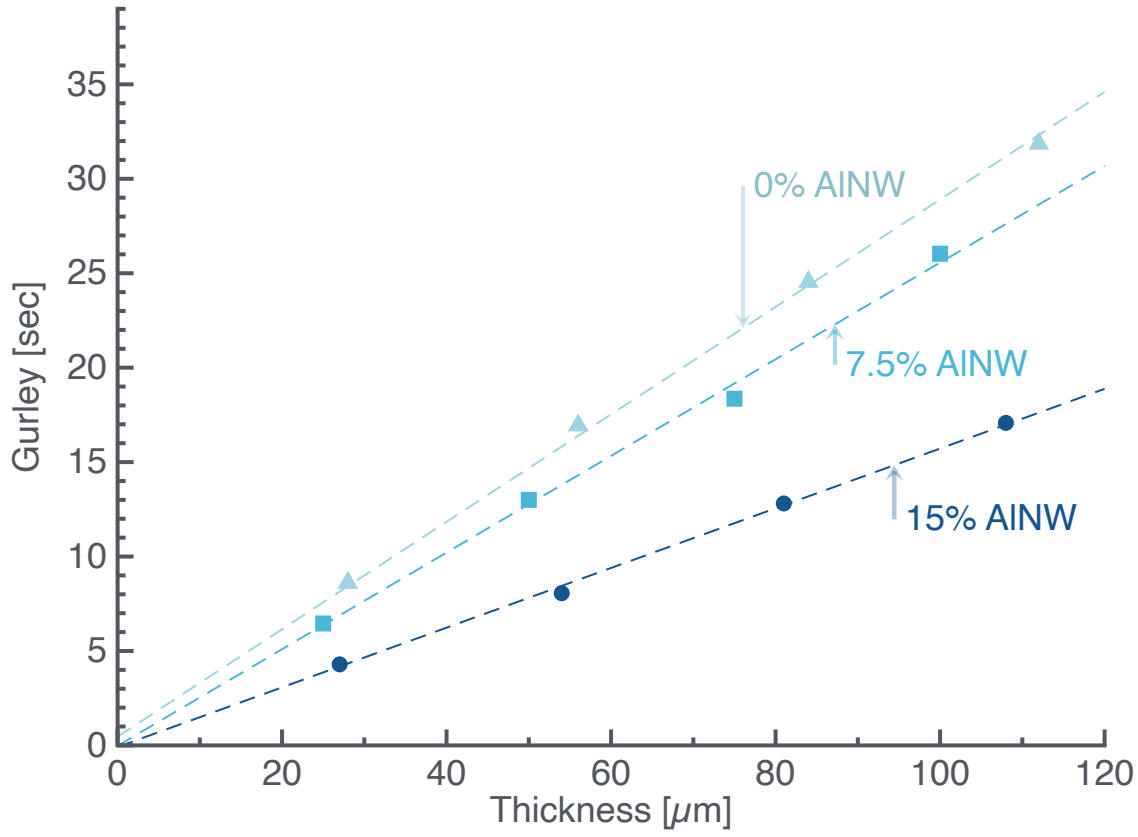

Figure 13: Air permeability (Gurley number) measurement of 0% AlNW, 7.5% AlNW, and 15% AlNW membranes. N=3, and the average reading of 300 cc of air passed through the membrane was taken to obtain the equivalent 100 cc measurement.

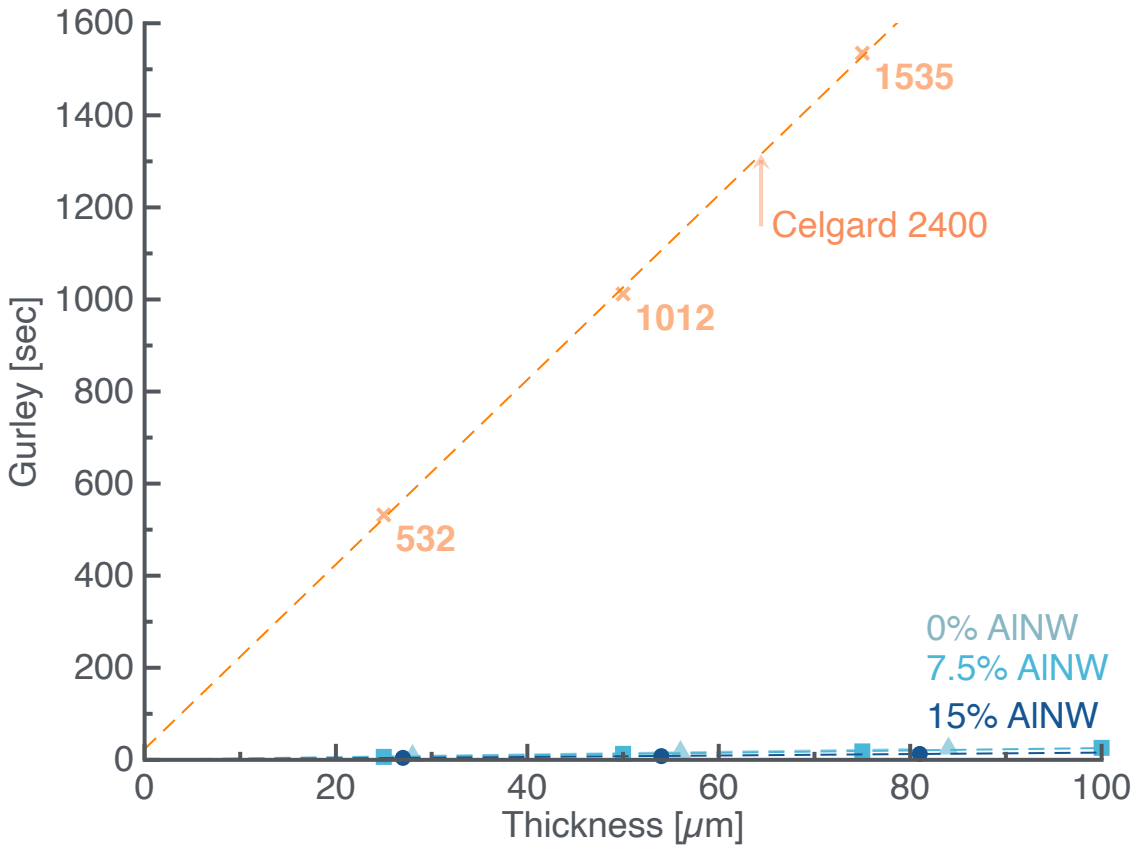

Figure 14: Air permeability (Gurley number) measurement of 0% AlNW, 7.5% AlNW, and 15% AlNW membranes compared to that of Celgard 2400. N=3, and the average reading of 300 cc of air passed through the membrane was taken to obtain the equivalent 100 cc measurement.

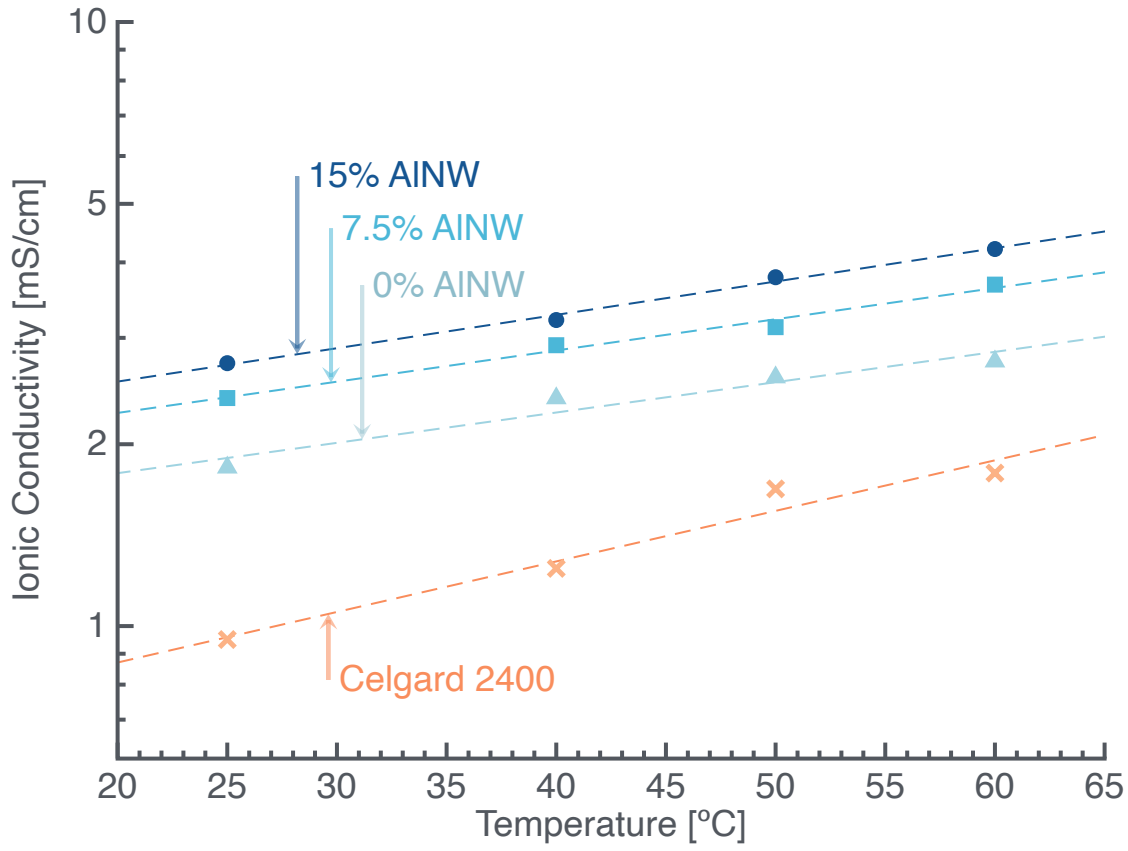

Figure 15: Ionic conductivity measurements of Celgard control, 0% AlNW, 7.5% AlNW, and 15% AlNW membranes as a function of temperature.

Wetting test results as shown in Figure 16 provide additional insight on the membranes' enhanced electrochemical performances. The area of electrolyte spread was recorded in ten second intervals after a 2μL drop of electrolyte was gently placed onto each membrane to evaluate their electrolyte absorption abilities. At 60 seconds, electrolyte only spread to 5% of the polypropylene membrane's 1.98 cm^2 total area. However, the electrospun membranes demonstrated substantially higher wettability at 75.0%, 81.4%, and 95.6% in total uptake for A0, A1, and A2 at the same mark of time. Such an increase of wettability could be attributed to the strong hydrophilic properties of both m-aramid and

AlNW as well as the increased porosity of the membranes. The carbonyl groups as well as amine groups in m-aramid increase hydrogen bonding between the polymer and carbonate electrolyte, promoting rapid uptake of the liquid. Alumina nanowires with very high surface dipoles further increase hydrogen bonding with electrolyte. As such, this investigation shows a marked increase of electrolyte wetting in polymer-ceramic nanocomposite membranes with over a 20 % increase in wetted area compared to that of neat m-aramid membranes. The nanocomposite's strong affinity to polar liquids further corroborate the increase in ionic conductivity as discussed above and propel its advantage further over its pure polymer counterpart.

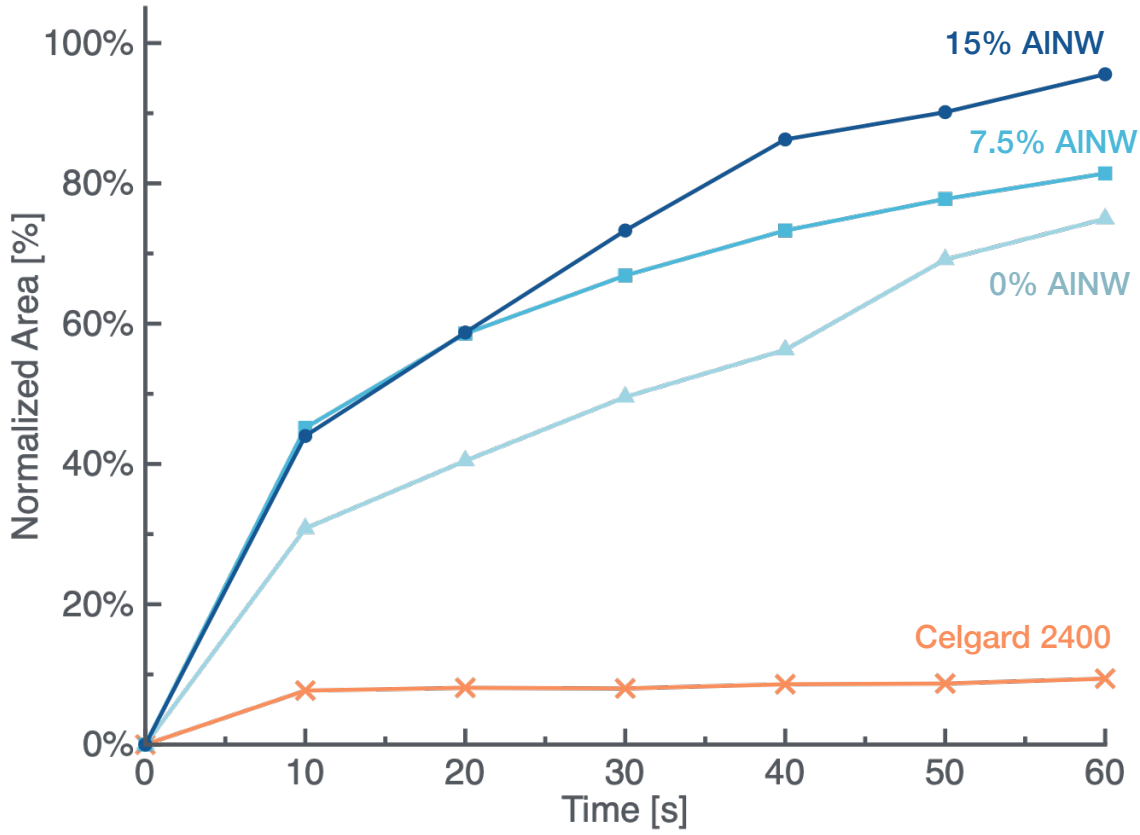

Figure 16: Wettability measurements of Celgard control, 0% AlNW, 7.5% AlNW, and 15% AlNW membranes over time. 2 µL of electrolyte (1M $LiPF_6$ in EC/DEC 1:1) was dropped on 1.98 cm^2 disc.

Increased ionic conductivity of the membranes also translated into superior cycling performance for lithium-ion battery full cells. In this study, we chose to quantify this gap in performance using full cells with lithium nickel cobalt manganese oxide $LiNi_{0.5}Co_{0.2}Mn_{0.3}O$ (NCM 523) as the working electrode (cathode, 155 mAh/g) and graphite as the counter electrode (anode, 330 mAh/g). Moderate areal capacity loadings were used to make sure the rate would be limited by the separator rather than the electrodes. Figure 17 plots five cycles of various C-rate cycling from 0.1C to 2C for a representative

15% AlNW cell as well as 0% AlNW and Celgard 2400 cells as foils. At a lower C-rate of 0.1C, the 15% AlNW and 0% AlNW cells demonstrated high average discharge capacities of 134 mAh/g and 132 mAh/g while the Celgard 2400 cell exhibited an average capacity of 112 mAh/g. This difference between m-aramid membranes and the control became exacerbated at 2C, the highest C-rate tested. The Celgard control was only able to output 40 mAh/g, while the 15% and 0% AlNW membranes maintained 85 and 79 mAh/g, respectively. When comparing the discharge capacities of the 0.1C cycles to the 2C cycles, Celgard 2400 retained only approximately 34% of its initial capacity. In contrast, approximately 64% and 59% of the original capacities were maintained for the 15% AlNW and 0% AlNW membranes. The nanocomposite membrane A2 exhibited the highest capacity retained with its superiority clearly emphasized in more demanding charge/discharge conditions. The difference in polarization in all three cells at 2C are shown in Figure 18. At a given capacity, the polarization of Celgard 2400 was noticeably higher compared those of the electrospun membranes, causing the cell to reach the specified cutoff potential of 4.2V sooner. Based on this data, we infer that ionic conductivities of the membranes are strongly tied to the corresponding full cell rate capabilities due to their contributions to ohmic voltage penalties. The polypropylene membranes yielded higher ohmic impedances that directly led to higher overpotentials at larger current densities, following an ohmic relationship. The m-aramid membranes in contrast reduced this impedance through its higher porosity and strong affinity to electrolyte, which in turn reduced polarization within the cell. Normalized capacity hysteresis curves for 2C rate cycling in supplementary Figure 19 shows that at 50% max capacity, the A2 cell exhibited a substantially lower hysteresis of 460 mV between its

charge and discharge cycle compared to the 750 mV gap of the polypropylene cell. Polarization decreased on average ~145 mV per charge and discharge step when comparing to the polypropylene control at this benchmark, allowing more complete utilization of the cathode active material capacity. This difference in observed performance at higher cycling rates suggests that the composite electrospun membrane impacts the ionic conductivity and diffusion of lithium ions in electrolyte less severely than the control separator does.

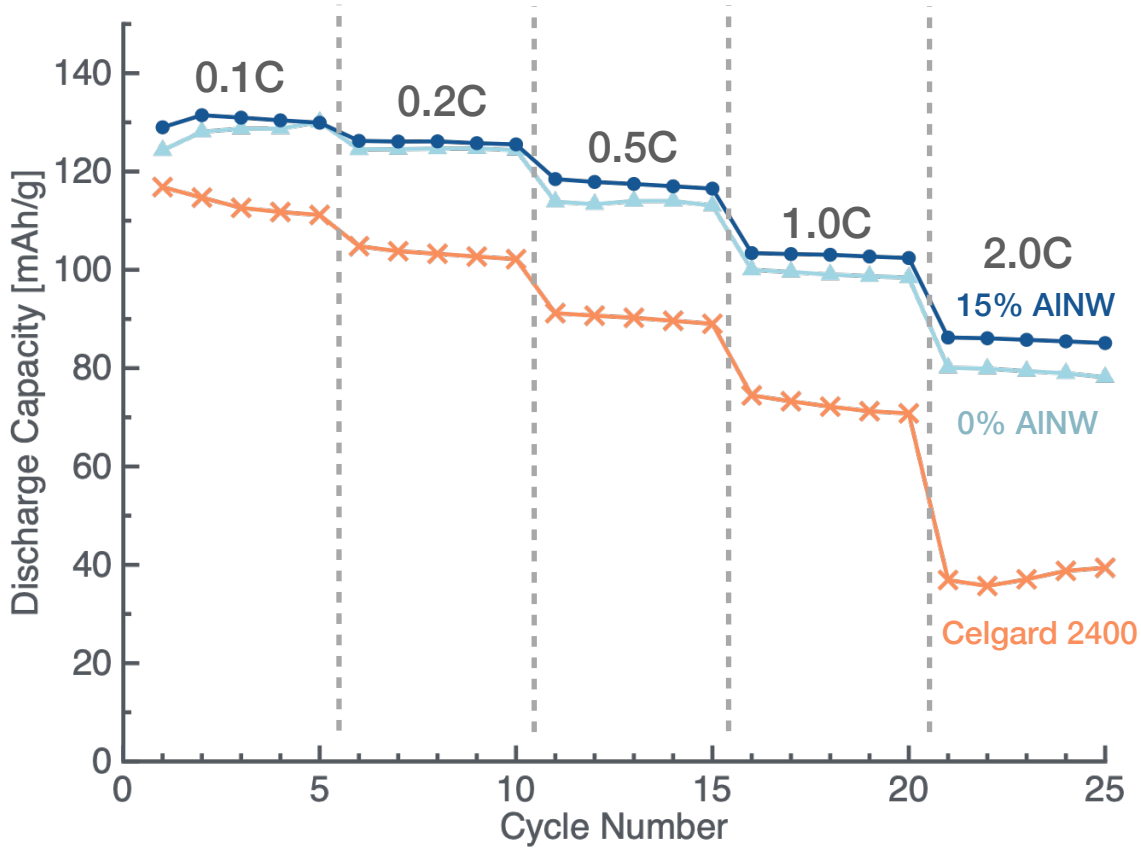

Figure 17: Rate capability testing of Celgard control, 0% AlNW, and 15% AlNW cells.

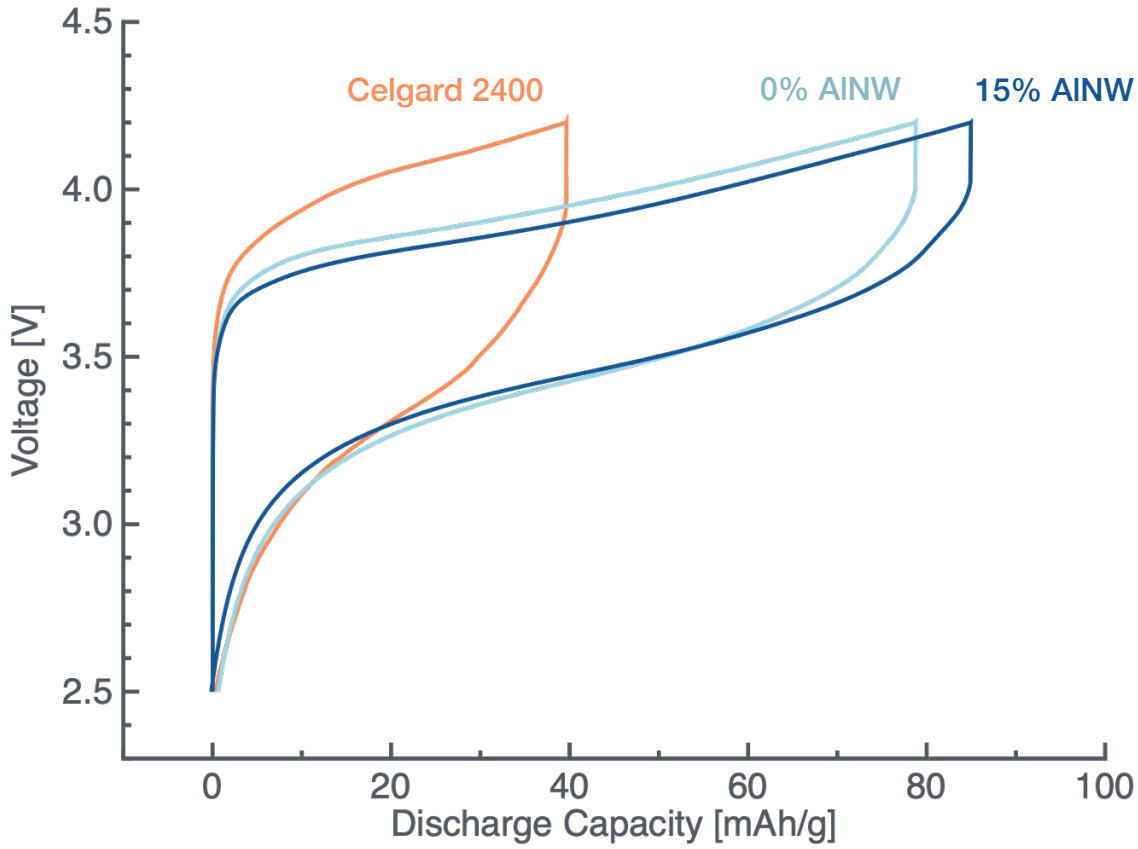

Figure 18: Hysteresis curves of Celgard control, 0% AlNW, and 15% AlNW cells tested at 2C.

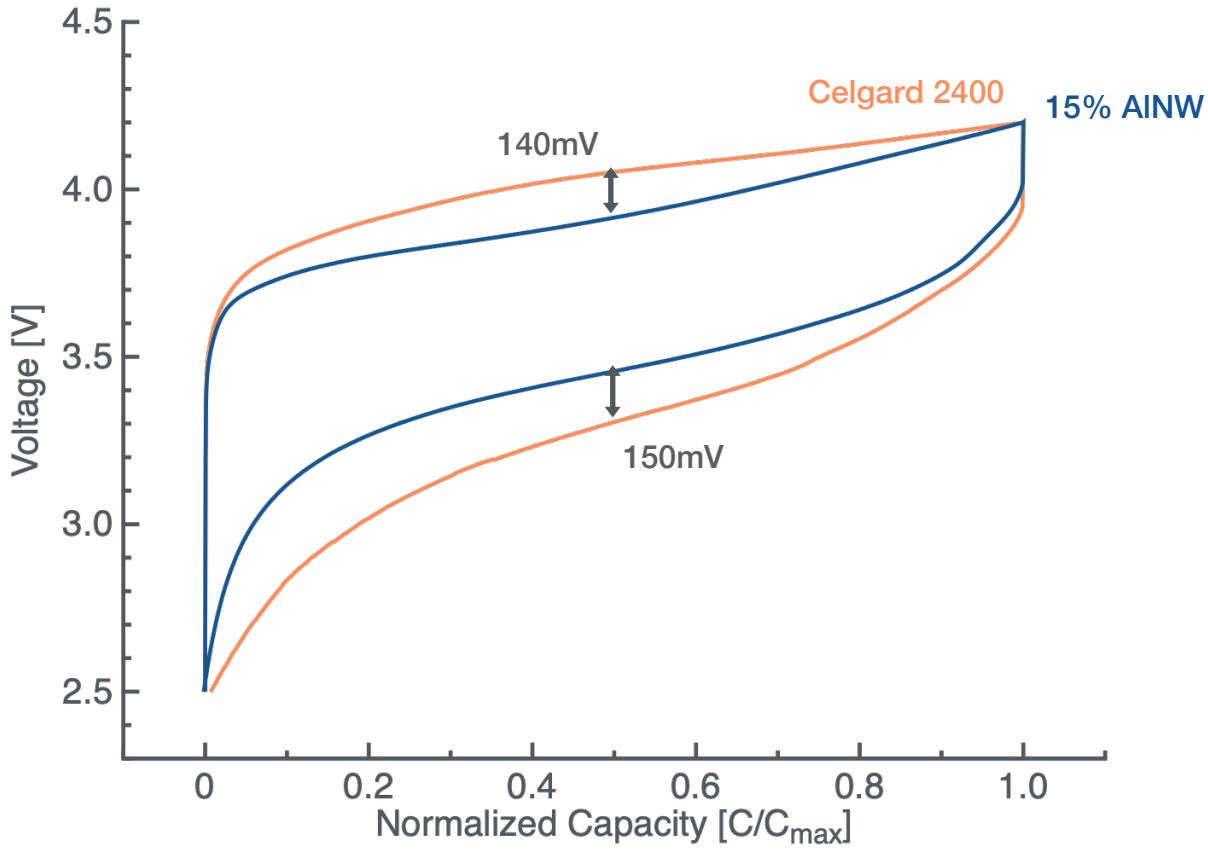

Figure 19: Normalized hysteresis curves of Celgard control, 0% AlNW, and 15% AlNW cells tested at 2C. Voltage difference measurements are taken at 50% of normalized capacity.

3.4 Conclusion

In this study, we demonstrated the successful fabrication of a thermally resistant nanocomposite separator with superb electrochemical properties for lithium-ion batteries. Incorporating alumina nanowires within nanofibers of electrospun m-aramid not only reduces area shrinkage near the polymer's glass transition temperature but also markedly enhance the admittance of the membrane within the context of impedance in an electrochemical system. Electrospun nanocomposite membranes exhibit excellent thermal

stabilities up to 250ºC (<10% area shrinkage below 250ºC) compared to the state-of-art ~120ºC. These electrospun membranes excelled in electrochemical performance, garnering an average of 145 mV reduction in polarization at 2C current densities compared to control values. As lithium-ion batteries integrate even further into the general populace's lives, developments as such must advance to protect users from catastrophic risk and ensure that energy and power demands are adequately met.

CHAPTER 4. CONCLUSION

The development of lithium-ion batteries has sustained substantial growth since its initial development in the late 20th century through significant material and electrochemical advances. Their base of use-cases continues to expand; lithium-ion batteries hold a competitive edge over other energy storage options owing to their superior energy densities for integration into vehicle electrification, renewable energy assets, consumer portable devices, and medical devices. However, limited charge and discharge rate capacities and the difficulty of minimizing the risk of thermal runaway by dendritic short-circuit reactions hinder the development of this energy storage system for aforementioned applications. On one hand, overpotential penalties causing a decrease in overall rate capability can be attributed to electrochemical charge transfer kinetics, transport limitations (in electrolyte concentration gradients and lithium solid-state diffusion), and ohmic resistance manifested in electronic or ionic resistance. On the other hand, the ability to segregate an electrochemical cell's cathode and anode through adverse conditions of temperature and mechanical stress to prevent short-circuiting dictates a cell's effectiveness in minimizing the risk of thermal runaway. Of these two considerations, the separator greatly influences the overpotential due to ohmic/concentration losses and the safety of an electrochemical cell. Separators derived from polypropylene and polyethylene blends often exhibit low glass transition temperatures (165ºC and 135ºC); creating a multilayer composite of the two allows a separator to close its pores at elevated temperatures which mitigates the risk of thermal runaway caused by shutting down the transport of ions. However, safety issues persist with this class of separators. An alternate strategy for maintaining safety for

separators involves improving the thermal stability of the separator material itself to prevent thermal shrinkage and subsequent short-circuiting of the electrodes.

The figures of merit to evaluate the candidacy of new separator materials commonly include electrochemical/chemical stability, ionic conductivity (taken from metrics such as electrolyte uptake, wettability, and porosity), thermal stability or shutdown capability, and mechanical strength (tensile, compression, or otherwise).

Electrospinning consists of a technique that forms ultrafine fibers through the uniaxial stretching of a viscoelastic polymer solution. This process, in contrast to other traditional fiber spinning methods, uses electrostatic forces to stretch the fibers mid-air as solvent evaporates and solidifies the solution. For this fiber to be propelled from an electrospinning spinneret, a critical voltage threshold must be reached so that the charge of the solution is greater than its surface tension; doing so forces a stream of solution to depart from the spinneret tip. The fibers that result from this method of deposition are deposited onto a current collector in the form of a non-woven mat. Fibers produced from this method often exhibit dramatically smaller diameters than those produced by conventional fiber spinning methods; it is typical to observe anywhere from tens to hundreds of nanometers in diameter. Electrospinning has gained considerable attention in the lithium-ion battery space, as the production of ultrafine fibers allows for battery separators with nano-scale pores and desirable properties such as increased wettability and electrolyte retention. Utilization of this technique could prove to be immensely valuable in creating next generation battery separators due to the method's ability to produce separators with high electrolyte uptake, wettability, and versatility due to the selection of polymers available to electrospin. One promising class of materials are aramids, which exhibit high

decomposition temperatures as well as mechanical properties. However, current work, both in this study as well as others, have found that the mechanical strength of m-aramid decreases significantly when electrospun into a porous membrane. This decrease can partly be explained through a geometric argument: the effective cross-area of the membrane decreases as porosity increases. As shown in this study, the porosity of electrospun membranes typically result in anywhere from 70-90% porosity, severely effecting the amount of bearable tensile load. However, further work has shown that the semi-crystalline m-aramid polymer reverts to an amorphous phase after dissolution into DMAc solvent and electrospun[76]. Recent advances demonstrate methods such as constrained annealing or solvent-assisted heat treatment to reintroduce crystalline domains within the electrospun membrane but have been limited to ultra-thick mats of m-aramid (1000 to 2000-micron thicknesses)[76,77]. Future work should pursue these concepts in further improving the mechanical properties of electrospun composite membranes for lithium-ion batteries.

REFERENCES

1. Tryggestad, C.*, et al.*, Global Energy Perspective 2019: Reference Case; McKinsey Energy Insights2019

2. Polymeneas, E.*, et al.*, Less carbon means more flexibility: Recognizing the rise of new resources in the elcectricity mix; McKinsey & Company2018

3. Frankel, D.*, et al.*, The new rules of competition in energy storage; McKinsey & Company2018

4. Maire, F., and Kramarchuk, R., US battery installs to accelerate strongly beyond 2020, but new risks emerge. *Platts S&P Global* 2019

5. Zanini, M.*, et al.*, *Carbon* (1978) **16** (3), 211

6. Mizushima, K.*, et al.*, *Materials Research Bulletin* (1980) **15** (6), 783

7. Nitta, N.*, et al.*, *Materials Today* (2015) **18** (5), 252

8. Ge, M.*, et al.*, *Nano Lett* (2012) **12** (5), 2318

9. Magasinski, A.*, et al.*, *Nat Mater* (2010) **9** (4), 353

10. Yao, Y.*, et al.*, *Nano Lett* (2011) **11** (7), 2949

11. Lin, D.*, et al.*, *Nat Nanotechnol* (2017) **12** (3), 194

12. Zhang, S. S., *Journal of Power Sources* (2006) **162** (2), 1379

13. Fuller, T., and Harb, J., *Electrochemical Engineering*. Wiley: 2018

14. Yang, M., and Hou, J., *Membranes (Basel)* (2012) **2** (3), 367

15. Orendorff, C. J., *The Electrochemical Society Interface* (2012) **21** (2), 61

16. Choi, S.-S.*, et al.*, *Electrochimica Acta* (2004) **50** (2), 339

17. Wang, Y.*, et al.*, *Journal of Membrane Science* (2017) **537**, 248

18. Croce, F.*, et al.*, *Journal of Physical Chemistry B* (1999) **103** (48), 10632

19. Croce, F.*, et al.*, *Nature* (1998) **394** (6692), 456

20. Choi, J.-A.*, et al.*, *Journal of Power Sources* (2010) **195** (18), 6192

21. Zhang, Y., *et al.*, *Journal of Membrane Science* (2016) **509**, 19

22. Abraham, K. M., *Electrochimica Acta* (1993) **38** (9), 1233

23. Arora, P., and Zhang, Z., *Chemical Reviews* (2004) **104** (10), 4419

24. Lee, H., *et al.*, *Energy Environ. Sci.* (2014) **7** (12), 3857

25. Zahn, R., *et al.*, *ACS Appl Mater Interfaces* (2016) **8** (48), 32637

26. Palacín, M. R., *Chemical Society Reviews* (2009) **38** (9), 2565

27. Heider, U., *et al.*, *Journal of Power Sources* (1999) **81-82**, 119

28. Jana, A., *et al.*, *Journal of Power Sources* (2015) **275**, 912

29. Djian, D., *et al.*, *Journal of Power Sources* (2007) **172** (1), 416

30. Love, C. T., *Journal of Power Sources* (2011) **196** (5), 2905

31. Appetecchi, G. B., *et al.*, *Electrochimica Acta* (1995) **40** (8), 991

32. Shi, Q., *et al.*, *Journal of Power Sources* (2002) **103** (2), 286

33. Kim, J. Y., *et al.*, *Electrochimica Acta* (2009) **54** (14), 3714

34. Ryou, M.-H., *et al.*, *Advanced Materials* (2011) **23** (27), 3066

35. Yu, T.-H., Trilayer battery separator. Google Patents(2000)

36. Yu, W.-C., and Hux, S. E., Method of making a trilayer battery separator. Google Patents(1999)

37. Zhu, Y., *et al.*, *Journal of materials chemistry A* (2013) **1** (26), 7790

38. Wei, J., *et al.*, *Journal of Power Sources* (2015) **294**, 494

39. Gomez, E. D., *et al.*, *Nano Letters* (2009) **9** (3), 1212

40. Yuan, R., *et al.*, *Macromolecules* (2013) **46** (3), 914

41. Ren, X., *et al.*, *Energy Technology* (2019) **7** (9), 1900064

42. Yang, C., *et al.*, *Journal of Power Sources* (2009) **189** (1), 716

43. Miao, Y.-E., *et al.*, *Journal of Power Sources* (2013) **226**, 82

44. Yanilmaz, M., *et al.*, *Electrochimica Acta* (2014) **133**, 501

45. Hao, J., *et al.*, *Journal of membrane science* (2013) **428**, 11

46. Zhang, X., *et al.*, *Polymer Reviews* (2011) **51** (3), 239

47. Lee, H., *et al.*, *Journal of Applied Polymer Science* (2013) **129** (4), 1939

48. Shrestha, R., *et al.*, *Nature communications* (2018) **9** (1), 1664

49. Rutledge, G. C., and Park, J. H., Gel-electrospinning process for preparing high-performance polymer nanofibers. Google Patents(2019)

50. Liao, X., *et al.*, *Science* (2019) **366** (6471), 1376

51. Li, D., and Xia, Y., *Advanced materials* (2004) **16** (14), 1151

52. Agarwal, S., *et al.*, *Electrospinning: A Practical guide to nanofibers*. Walter de Gruyter GmbH & Co KG: 2016

53. Doshi, J., and Reneker, D. H., *Journal of electrostatics* (1995) **35** (2-3), 151

54. Jaeger, R., *et al.*, Electrospinning of ultra-thin polymer fibers. In *Macromolecular symposia*, Wiley Online Library(1998), Vol. 127, pp 141

55. Yarin, A. L., *et al.*, *Journal of applied physics* (2001) **90** (9), 4836

56. Xue, J., *et al.*, *Chemical reviews* (2019) **119** (8), 5298

57. Liu, K., *et al.*, *Sci Adv* (2017) **3** (1), e1601978

58. Forward, K. M., and Rutledge, G. C., *Chemical Engineering Journal* (2012) **183**, 492

59. Bazhenov, S., *Journal of materials science* (1997) **32** (15), 4167

60. Young, R., *et al.*, *Journal of materials science* (1992) **27** (20), 5431

61. Aramid by Teijin. p 9

62. Li, J., *et al.*, *Journal of Applied Polymer Science* (2016) **133** (30)

63. Yao, L., *et al.*, *Fibers and Polymers* (2010) **11** (7), 1032

64. Mazzocchetti, L., *et al.*, Poly-m-aramid nanofiber mats: Production for application as structural modifiers in CFRP laminates. (2016)

65. Lee, J. H., *et al.*, *Journal of Nanoscience and Nanotechnology* (2016) **16** (10), 10724

66. Armand, M., and Tarascon, J.-M., *nature* (2008) **451** (7179), 652

67. Xia, Y., *et al.*, *Advanced Materials* (2003) **15** (5), 353

68. Tian, B.*, et al.*, *nature* (2007) **449** (7164), 885

69. Lei, D.*, et al.*, *Science* (2017) **355** (6322), 267

70. Kim, S. J., and Jang, H., *Tribology international* (2000) **33** (7), 477

71. Jin, L.*, et al.*, *Journal of Fiber Bioengineering and Informatics* (2011) **4** (3), 245

72. Varga, K.*, et al.*, *Lenzinger Berichte* (2011) **89**, 50

73. Horn, M.*, et al.*, Strength and durability characteristics of ropes and cables from Kevlar® aramid fibers. In *OCEANS'77 Conference Record*, IEEE(1977), pp 313

74. Lewicki, J. P.*, et al.*, *Scientific Reports* (2017) **7** (1), 43401

75. Li, H.*, et al.*, *Adv Mater* (2017) **29** (44)

76. Ryu, S.-Y.*, et al.*, *European Polymer Journal* (2017) **91**, 111

77. Chung, J., and Kwak, S.-Y., *European Polymer Journal* (2018) **107**, 46